Origin of Intraseasonal Variability in the Eastern Equatorial Indian Ocean: Intrinsic Variability, and Local and Remote Wind-Stress Forcings

(赤道東インド洋の季節内変動の起源：内在的変動、遠方および局所的な風応力強制)

Thesis for a Doctorate

Chorong Lee

李　チョロン

Department of Natural History Sciences, Graduate School of Sciences,

Hokkaido University, Sapporo, 060-0810, Japan

北海道大学大学院理学院自然史科学専攻

September 2017

Abstract

Eastern equatorial Indian Ocean (EEIO) experiences large intraseasonal variability (ISV), which arises from intrinsic variability and also is induced by local and remote atmospheric forcings. We investigate the relative contributions of intrinsic variability and local and remote forcings to ISV in EEIO by conducting a set of numerical model experiments using Regional Ocean Model System over the Indian Ocean with grid interval of 0.25° in longitudes and latitudes. In the control run, the model is forced year-to-year varying forcings for 20 years (1996–2015). We account the first 10 years as the necessary period to spin up. The control run can reproduce realistic ISV in EEIO.

To distinguish ISV originating from intrinsic variability and that caused by atmospheric forcings, we examine three experiments with different perturbation at the beginning of 10-year integration (2006-2015). The ensemble-mean of these experiments represents forced responses, while differences among the experiments indicate the intrinsic variability. In the central to eastern equatorial Indian Ocean, forced oceanic ISV is much larger than intrinsic ISV in the whole 500 m depth. For ISV of sea surface temperature, atmospheric forcings play a larger role than intrinsic variability in the most region of the Indian Ocean. Atmospheric forced ISV distinctly penetrates to the subsurface in EEIO.

To understand a relative role of atmospheric forcings, especially that of wind-stress, four regional forcing experiments are conducted. In the first two experiments, wind-stress ISV is retained over western (west of 80°E) or eastern (east of 80°E) region, while in the other two experiments the latter forcing region is further subdivided into middle eastern (80°–100°E) and far eastern (east of 100°E) regions. At the surface, local forcing, especially in the middle eastern Indian Ocean, dominates ISV in EEIO. In the subsurface, remote forcing also plays an important

role in ISV. Below the thermocline, the influence of wind forcing from the west of 80°E cannot be neglected on ISV, even work constructively with that from the east of 80°E. The contribution of wind forcing east of 100°E is small but cannot be ignored near the Java coast.

Table of Contents

Abstract

1. Introduction..5

2. Methods..10

    2.1. Model..10

    2.2. Experiments..11

    2.3. Data sets..12

3. Results..15

    3.1. Comparison between model and observations..15

    3.2. Intrinsic and forced ISV..16

    3.3. Regionally forced ISV..19

4. Summary and Discussion..23

Acknowledgements..28

References..29

Table..38

Figures..39

1. Introduction

Oceanic variables in the eastern equatorial Indian Ocean (EEIO) exhibit considerable intraseasonal variability (ISV) about 30-90 days period. ISV of Sea Surface Temperature (SST) in EEIO with dominant period of 30-70 days is 40% of total SST variability, and plays important role in air-sea interaction (Zhang 2005; Saji et al. 2006; Duncan and Han 2009; DeMott et al. 2015; Horii et al. 2015). ISV of Sea Surface Salinity (SSS) also explains more than 25% of the total nonseasonal variability over much of the Indian Ocean (Guan et al. 2014; Horii et al. 2015; Li et al. 2015). Sea Surface Height (SSH) observed by both satellite and tidal gauges at the Sumatra and Java coasts has distinct peaks at 30-60 days and 90 days (Han 2005; Oliver and Thompson 2010; Iskandar et al. 2014; Horii et al. 2016). ISV of the mixed layer depth along the equatorial Indian Ocean is even larger than seasonal variability, affecting SST and the primary productivity and the timing of phytoplankton blooms (Keerthi et al. 2012; Keerthi et al. 2015; Schiller and Oke 2015). Intraseasonal upwelling in EEIO also can change not only the variability of chlorophyll concentration but mean of that (Jin et al. 2012a; Jin et al. 2012b; Chen et al. 2015). Dominant 30-70 days ISV of zonal velocity is observed by mooring in EEIO (Iskandar and McPhaden 2011; Iskandar et al. 2014). The largest ISV of zonal velocity occurs at the surface, but it penetrates vertically below the thermocline. Recent seaglider observation captured ISV of temperature, salinity, and even oxygen propagates down to 1000 m linked to Rossby wave in the central equatorial Indian Ocean (Webber et al. 2014).

ISV can arise intrinsically without intraseasonal external forcing. Many studies examine how large the intrinsic variability is by comparing the numerical model results with and without ISV of external forcing. Intrinsic ISV is strong near the western boundary of the Indian Ocean, the south of Java, and the south of Sri Lanka (Sengupta et al. 2001; Feng and Wijffels 2002; Brandt et al. 2003; Han 2005; Yu and Potemra 2006; Palastanga et al. 2007; Ogata et al. 2008; Zhou et al. 2008; Ogata and Masumoto 2011). The instability developing from baroclinic and barotropic energy conversions can alter by the characteristics of current, such as volume transport, temperature, and salinity, and spatial gradient of density are important factors (Yu and Potemra 2006; Ogata and Masumoto 2011). Yu and Potemra (2006) revealed that intrinsic variability in the south of Java depends on the magnitude of mean wind-stress, even though they use monthly mean climatological wind fields averaging over different period.

Intraseasonal atmospheric forcings also cause oceanic ISV locally and remotely. Local responses are mostly trapped in mixed layer, and observed in SST and SSS (Harrison and Vecchi 2001; Duvel et al. 2004; Saji et al. 2006; Chen et al. 2015; Raj Parampil et al. 2016). On the other hand, remote responses may be more clearly seen in subsurface temperature, current velocity and SSH, especially in EEIO via equatorial wave dynamics (Han 2005; Iskandar 2005; Oliver and Thompson 2010; Schiller et al. 2010; Iskandar and McPhaden 2011; Nagura and McPhaden 2012; Horii et al. 2016). Schiller et al. (2010) suggested that 60-day fluctuation of subsurface temperature from the central equatorial Indian Ocean to Indonesian Sea is the result of free Kelvin and Rossby waves caused by zonal wind-stress in EEIO. ISV of zonal velocity at the thermocline depth propagates east-upward with a broad range of phase speeds expected for the first three baroclinic equatorial Kelvin waves (Iskandar and McPhaden 2011). Nagura and McPhaden (2012) using linear continuously stratified model suggested that ISV of SSH in EEIO mostly represented by first two baroclinic Kelvin waves and first meridional mode Rossby wave. These waves propagate zonally and downward.

Several numerical studies for ISV in the Indian Ocean employed experiments in which specific forcing variables of fluxes are retained and other are suppressed (Duncan and Han 2009;

Li et al. 2014; Chen et al. 2015; Li et al. 2015). For example, Li et al. (2015) conducted a series of experiments in which either of wind-stress, wind speed (the latter for turbulent heat fluxes), shortwave radiation, or precipitations is suppressed on intraseasonal timescales by using low-pass filters, in addition to their standard run, in which all forcings are applied. They concluded that wind-stress is a primary factor driving ISV of SSS in the equatorial region. Other studies on ISV of SST and SSH with similar numerical experiments also revealed that the effect of wind-stress ISV on oceanic ISV is primary or secondary over all atmospheric forcings.

Much study has been investigated relative importance of local and remote atmospheric forcings by using lag-correlation, coherency-phase analyses or numerical model. Iskandar and McPhaden (2011) argued that ISV of zonal velocity below the thermocline leads both that near the surface and ISV of local wind-stress using mooring observation at 0°, 90°E. Chen et al. (2015), who conducted a regional forcing experiment in which intraseasonal atmospheric forcings are suppressed over the southeastern equatorial Indian Ocean (10°S-0°, 95°E-114°E), compared the results of the regional forcing experiments with those of a standard experiment for which forcings are applied for the whole domain. They concluded that ISV of SSH and thermocline depth in that region is mainly caused by equatorial Indian Ocean wind-stress which generate Kelvin waves propagating along the equator and subsequently along the Sumatra and Java coasts in boreal summer. They also found that ISV of SST in that region is mainly caused by local forcings.

Although our knowledge about mechanisms of ISV in EEIO has increased substantially in the last two decades, further studies are still needed in order to better understand ISV in EEIO. In particular, it is not comprehensively assessed the relative importance between intrinsic ISV and forced ISV in realistic setting where these two mechanisms occur simultaneously. Because the magnitude of intrinsic ISV is sensitive to climatological wind field, the comparison of the results with and without wind-stress ISV may not be sufficient. Also, regional forcing experiment employed by Chen et al. (2015) is a powerful method to identify influence remote and local forcings, but they conducted only one regional forcing experiment. Therefore, they suggested that zonal wind-stress over broad equatorial Indian Ocean at 20-day before is related to ISV of thermocline doeth in EEIO by lag-correlation. However, if one increases number of forcing regions and correspondingly the number of regional forcing experiments, one can obtain more detailed information of important forcing regions.

The purposes of this study, therefore, are two folds. One is to evaluate how much of ISV is forced responses or arise from the intrinsic variability under realistic atmospheric forcings, and the other is to identify the roles of wind-stress in various regions in the Indian Ocean in ISV in EEIO. We conduct three experiments changing spin-up length but forced by full atmospheric forcings and analyze both intrinsic and forced ISV in whole Indian Ocean. A natural approach to attain the second purpose is to conduct multiple regional forcing experiments. Thus, we also conduct a series of regional forcing experiments with wind-stress acting only in the western (west of 80°E), eastern (east of 80°E), middle eastern (80°-100°E), and far eastern (east of 100°E) Indian Oceans using Regional Ocean Modelling System (ROMS). In the regional forcing experiments, we only modify wind-stress forcings, because previous studies showed that wind-stress forcing is the most important in remote responses (Duncan and Han 2009; Iskandar and McPhaden 2011; Nagura and McPhaden 2012; Chen et al. 2015; Horii et al. 2016).

The rest of this paper is organized as follows. Section 2 describes model, numerical experiments and methods. In section 3, we explain the features of ISV in our model. This section is composed of three parts. In the first part, we briefly compare our model results with observation. In the second part, we examine a portion of intrinsic ISV of total ISV. In the last part, the regional forcing experiments are also compared with each other to clarify the most effective wind-stress affecting subsurface temperature variation in EEIO. Section 4 provides summary and discussion.

2. Methods

2.1. Model

The model used in this study is ROMS, which solves the primitive equations with terrain-following curvilinear coordinates (Song and Haidvogel 1994; Haidvogel et al. 2000; Shchepetkin and McWilliams 2005). The domain of model covers the entire Indian Ocean (30°S-120°E, 45°S-30°N) with a horizontal grid-spacing of 0.25° by 0.25° and 40 sigma layers (Fig. 1). This horizontal resolution is commonly used in recent papers investigating ISV in the Indian Ocean (e.g. Li et al. 2014; Chen et al. 2015; Li et al. 2015). For the advection, third-order upstream horizontal advection and fourth-order centered vertical advection schemes are used (Shchepetkin and McWilliams 2005). Harmonic horizontal mixing is applied to the temperature and salinity along the isopycnal surface. The shortwave radiation is absorbed as a function of depth by Paulson and Simpson (1977). For the momentum, biharmonic horizontal mixing is used along the constant sigma surface. The local turbulent closure schemes based on the level 2.5 turbulent kinetic equations (Mellor and Yamada 1982) and the Generic Length Scale parameterization (Umlauf and Burchard 2003) are applied for vertical mixing. Quadratic drag is activated for bottom friction.

The model has open boundaries along southern, western, and eastern boundaries at 45°S, 30°E, and 120°E, respectively. From those open boundaries, the three dimensional temperature, salinity, and velocity radiate outward, while they are also nudged to outside values. For inflows (outflows), nudging timescale is 5-day (150-day). The surface elevation propagates out of domain with the shallow-water wave speed (Chapman 1985). This is known to be useful when using Flather condition on the two dimensional momentum. Flather condition is that the difference of barotropic velocity between modeled value and exterior value radiates out of domain at the external gravity wave speed (Flather 1976). Chapman and Flather conditions are necessary to apply tidal forcing from the open boundary.

For control run (CNTL), the model was integrated for 20 years with year-to-year varying forcing data that contains ISV from 1 January 1996 to 31 December 2015. Model outputs were 3-day average values, and were filtered with a 20-120 day band-pass filter (the 4th order butterworth filter) to obtain ISV. To analyze the data for which mean circulation and forced ISV are well developed and to avoid end effects of band-pass filter, we analyzed only 7 years data from 3 September 2008 to 31 August 2015.

2.2. Experiments

In order to understand the mechanisms of ISV in EEIO, we conducted two sets of experiments. In one set of experiments, we integrate another two ensembles in addition to CNTL to evaluate the importance of intrinsic and forced ISV (Table 1). CNTL is regarded as 1st ensemble. For the 2nd (3rd) ensemble, we integrate the last ten years starting from 1 January 2006 from the condition of December 2004 (2003). At the beginning of the 10-year integration, the different perturbations should yield different ISV arising from the intrinsic variability, though forced responses should be the same among ensembles. Therefore, by comparing the magnitudes of differences and those of ensemble mean, we can evaluate the importance of the intrinsic and forced ISV.

In the other set of experiments, to understand a role of wind-stress forcings in the different regions in oceanic ISV, we conducted four regional forcing experiments, in which ISV of wind-stress retains only in respectively selected domains (Table 1). As introduced in section 1, wind-stress forcings are important in the remote ISV responses (Duncan and Han 2009; Iskandar and

McPhaden 2011; Nagura and McPhaden 2012; Chen et al. 2015; Horii et al. 2016). Regions are separated only zonally; this is because if we also separate regions meridionally, artificially strong wind-stress curl could occur along the southern and northern edges of the regions associated with the strong zonal wind stresses and small meridional length scale of them. First, we divide the Indian Ocean into two parts; west of 80°E (Western Forcing run; WF) and east of 80°E (Eastern Forcing run; EF). In WF, ISV of wind-stress is retained only in the west of 80°E, and ISV of wind-stress in the east of 80°E is suppressed by a 20-120 day band-stop butterworth 4th order filter. With the same manner, ISV of wind-stress only to the east of 80E is retained in EF. These two experiments can help us to figure out a role of wind-stress in each basin in three-dimensional structures of ISV in EEIO. Second, the eastern basin is further divided into two parts; in Middle Eastern Forcing run (MidEF) wind-stress ISV only in 80°-100°E is retained, while in Far Eastern Forcing run (FarEF), wind-stress ISV east of 100°E is retained. The 100°E longitude is very close from the longitude where the Sumatra western coast or the eastern boundary of the Indian Ocean crosses the equator. The model run that is forced atmospheric ISV over the whole domain is referred to as Full Forcing run (FF) in the context of the regional forcing experiments, and is the same as CNTL.

2.3. Datasets

The following dataset are used for the model integration. The temperature and salinity initial condition is based on climatological 1° by 1° temperature and salinity of Northern Indian Ocean Atlas, which is improved compared with the World Ocean Atlas 2009 by Chatterjee et al. (2012). Japanese 55-year Reanalysis data for Driving Ocean-sea ice models (JRA55-DO) (personal communication Dr. H. Tsujino) are used for surface forcings on a 0.5° grid in longitude and latitude at 3-hour temporal interval. JRA55-DO is an optimized dataset for ocean and ice model forcings based on Japanese 55-year Reanalysis (Harada et al. 2016; Kobayashi and Iwasaki 2016), and the successor of COARE2 forcing dataset (Webster and Lukas 1992). We use 10 m winds, 10 m air temperature, 10 m specific humidity, sea surface pressure, shortwave and downward longwave radiation, and precipitation. Heat and freshwater fluxes at the surface were calculated model run using above variables and model SST by bulk formula (Fairall et al. 2003). Although ROMS can calculate wind-stress similarly, we calculated wind-stress using JRA55-DO variables by the same bulk formula before model run in order to control ISV of wind-stress for regional forcing experiments. Aforementioned nudging at the open boundaries are based on the monthly 1° by 1° temperature, salinity, velocity and SSH of Ocean Reanalysis System 4 (ORAS4) provided by European Centre for Medium-Range Weather Forecasts (Mogensen et al. 2012; Balmaseda et al. 2013). For tidal forcing, the tidal solution simulated by Oregon State University is used (Egbert and Erofeeva 2002). The monthly climatological river discharges estimated by Dai and Trenberth (2002) are applied as point sources on the land-sea boundary.

We compare our model results with the several observational datasets. The climatological distributions of temperature, velocity, and the mean thermocline depth at the surface are examined using the Simple Ocean Data Assimilation version 2.2.4 (SODA) from January 1981 to December 2010 (Carton 2005; Carton and Giese 2008). It is long-term monthly ocean reanalysis product on a 0.5° by 0.5° horizontal grid. The Optimum Interpolation Sea Surface Temperature version 2 (OISST), on a 0.25° by 0.25°grid and daily temporal interval, is used to analyze ISV of SST (Reynolds et al. 2007; Banzon et al. 2016). SSH data of Archiving, Validation, and Interpretation of Satellite Oceanographic data (AVISO) with daily 0.25° by 0.25° horizontal resolution is also used (Le Traon et al. 1998; Ducet et al. 2000). We also examine climatological nitrate concentration in World Ocean Atlas 2009 (Garcia et al. 2010). Nitrate is one of the most important nutrients for phytoplankton photosynthesis. Because nitrate in the euphotic zone, the layer of sea water that receives enough sunlight for photosynthesis to occur, is consumed by phytoplankton, its concentration sharply increases with depth as known as nitracline. Nitracline along the equatorial band is located around 100 m depth (Fig. 2), which is similar to the thermocline depth (Figs. 3ef). ISV near the nitracline can influence the vertical supply of nutrients to the surface, and can even promote plankton bloom (Waliser et al. 2005; Resplandy et al. 2009; Jin et al. 2012a; Jin et al. 2012b). Therefore, we pay our attention to ISV around 100 m, which can be important in marine ecosystem.

3. Results

3.1. Comparison between model and observations

Before we describe modeled ISV, we briefly compare climatology between ensemble-mean (EM) and observation (Fig. 3). In boreal summer, Somali Current and Summer Monsoon Current near Sri Lanka are distinct. Cold temperature in the western boundary is contrasted to warm pool, which is well developed around the eastern boundary. Low temperature along the Java and Sri Lanka coasts is induced by seasonal upwelling. Near the eastern tip of Africa continent, temperature is also low due to the divergence of surface water by a clockwise Great Whirl and anticlockwise Somali Gyre, which emerge off the coast of Somalia (Schott and McCreary 2001). In boreal winter, strong westward zonal current, North Equatorial Current is developed to the north of the equator. In the south of the equator, Equatorial Counter Current flows eastward. The zonal temperature gradient in winter becomes smaller than that in summer. Our model well simulated these seasonal spatial patterns of currents and temperature, except the current speed in winter. The southward flow in southwestern Indian Ocean almost disappears in EM. This bias contributes decreasing the magnitude of other currents in whole basin especially in the western equatorial Indian Ocean. Annual mean 20°C isotherm depth, which is often used as a thermocline depth in the tropical Indian Ocean, is also compared (Figs. 3ef). Both observation and model indicate that the isotherm depth is shallow in the southwestern tropical Indian Ocean, which is called Seychelles Chagos thermocline ridge. By contrast, in the northern Indian Ocean the isotherm is deep. This meridional gradient of the isotherm is slightly larger in model than that in observation.

Not only mean fields but also spatial structure of standard deviation (STD) of SST and SSH ISVs generally agree well with observation (Fig. 4). ISV of SSH in both satellite observation and EM is large in the Great Whirl region, the south of Java, and the west of Madagascar, where eddy activity is high. Along the equatorial band, ISV of SSH is low except near the Sumatra coast. STD of SST ISV in model has a similar pattern and magnitude to those in satellite observation. The high ISV of SST exist in active upwelling region; the Great Whirl region, the south of Java, the Seychelles Chagos thermocline ridge.

3.2. Intrinsic and forced ISV

In this subsection, we examine intrinsically originating ISV and forced ISV, based on ensemble experiments described in section 2.1. To do so, it is useful to define intrinsic variance ratio (IVR), the variance of differences from the ensemble mean divided by variance of CNTL follows:

$$\mathrm{IVR}(x,y,z)=\frac{\frac{1}{3}\sum_{m=1}^{3}\frac{1}{t_2-t_1}\int_{t_1}^{t_2}\left[u_m(x,y,z,t)-u_{EM}(x,y,z,t)\right]^2 dt}{\frac{1}{t_2-t_1}\int_{t_1}^{t_2}u_{FF}(x,y,z,t)^2\,dt}\times 100\ (\%) \qquad (1)$$

where, x, y, and z are zonal, meridional and vertical coordinate, t is the time, u is band-pass filtered variable of interest, u_m is the m'th ensemble, u_{CNTL} is the CNTL. If the IVR is larger (smaller) than 50%, ISV induced by intrinsic variability has larger (smaller) magnitude of the forced ISV.

Figure 5 shows IVRs of temperature and zonal velocity. At the surface, forced ISV of SST is larger than intrinsic ISV of SST (IVR<50%) in almost whole Indian Ocean. The area where IVRs of 100 m temperature are smaller than 50% becomes narrower at 100 m depth than that at the surface, and exists only along the equatorial band and the eastern boundary of the Indian Ocean (Fig. 5c). Along the 60°-100°E equatorial band and Sumatra, IVRs of 100 m temperature are smaller than 20%, indicating strong dominance of forced ISV. This region is suggested as the pathway of the equatorial and coastal Kelvin waves (Iskandar 2005; A. Schiller et al. 2010;

Iskandar et al. 2014). Along the southern coast of Java, IVRs of temperature at the surface are larger than that at 100 m depth, possibly related to steep SST gradient (Figs. 3bd). IVRs of temperature along 500 m isobar to the south of Sumatra and Java (equator-coast cross section in Fig. 1) illustrate that the effect of external forcing can penetrate to the subsurface (Fig. 5e). ISV of temperature in upper 200 m layer along the 70°-100°E equatorial band is overwhelmed by atmospheric forcing effects. Such strong dominance of atmospheric forcings is also found even at levels deeper than 500 m depth near the eastern boundary. The minimum of IVRs is located at the depth range of 50-150 m in EEIO. The forced response of zonal velocity ISV is larger than the unforced response along the equator and the eastern boundary of Indian Ocean at both the surface and 100 m depth (Figs. 5bd). The high IVRs of zonal velocity (>70%) appear in the western boundary region and the southeastern Indian Ocean, consistent with the previous study (e.g. Sengupta et al. 2001; Brandt et al. 2003; Han 2005; Yu and Potemra 2006; Ogata et al. 2008). The region, where IVRs of zonal velocity ISV are smaller than 20%, becomes much narrower at 100 m depth than that at the surface; 70°-90°E at 100 m depth (Figs. 5d). IVRs of zonal velocity along the equator-coast cross section indicate that the intraseasonal forced response of zonal velocity overwhelms above the thermocline, especially in the longitude range of 65°-80°E (Fig. 5f). Around the 90°-95°E, the deep minimum of IVRs appear at 200 m. Both temperature and zonal velocity varying with intraseasonal timescales in EEIO are considerably forced by atmospheric forcings.

Figure 6 shows that correlation coefficients between modeled EM and observed ISV are closely associated with the dominance of the forced ISV in Fig. 5. The correlation coefficients of SSH between AVISO and model (Fig. 6a) are large along the central to eastern equatorial band (Figs. 6a), where forced ISV is overwhelming in subsurface depths (Figs. 5ce). Extratropical region shows low correlation coefficients, coinciding with the distribution of unforced responses.

The correlation map of SST shows that ISV of SST in the broad central equatorial region is well reproduced in our model (Fig. 6b). Off Sumatra correlations are generally small but IVR (Fig. 5) shows that forced ISV is dominant and in most cases overwhelming. So "off Sumatra" appears to be contradicting from general rule of this is rather ISV of SST between model and observation has weak relation off the Sumatra. This is also because of large intrinsic ISV in this region (Fig. 5).

It is also instructive to compare distribution of ISV STD (Fig. 7) with the IVR shown in Fig. 5. STD of 100 m temperature ISV is strong in EEIO and near western boundaries. The latter regions roughly correspond to regions where intrinsic ISV is dominant. Such simple relation is not seen in EEIO, but the strong ISV STD in EEIO distributes both regions where forced ISVs are strong or weak. In the equator-coast cross section, STD of temperature ISV is strong in 50-150 m depth range over the equator slightly above 20°C isotherm. The depth range becomes wider along the Sumatra and Java coast probably associated with large displacements of 20°C isotherm in season (Figs. 17cd). The zonal velocity at 100 m has large ISV along the equator with the local maximum at 83°E and the south of Java coast (Fig. 7b). ISV of zonal velocity along the equator is concentrated above the thermocline (Fig. 7d).

Corresponding ISV of wind-stress over the tropical Indian Ocean is shown in Fig. 8. STD of ISV of zonal wind is larger than 0.015 N m^{-2} over 70°-90°E equatorial band, collocated to the aforementioned dominant forced ISV of zonal velocity at 100 m depth. In the south of the Sunda Strait and Java, zonal wind-stress has distinct ISV, which excesses 0.027 N m^{-2}. STD of meridional wind ISV around the Sunda Strait also has higher value than 0.015 N m^{-2}.

To obtain overall structure of forced ISV along the equator, we conduct Complex Empirical Orthogonal Function (CEOF) analysis for temperature ISV of upper 500 m depths over equatorial band of Indian Ocean (5°S-5°N; 35°E-115°E) from 3 September 2008 to 31 August 2015. ISV of temperature at all nine levels (0, 50, 100, 150, 200, 350, 300, 400, and 500 m) are weighted by square root of the layer thickness and combined as covariance matrix. Figure 9 shows spatial patterns and time series of the CEOF first mode of temperature in EM. The explained variance is 25.6%. The maximum amplitude occurs along the eastern boundary over whole depth range, and therefore this mode is closely related to upwelling near the Sumatra coast. At the surface, temperature ISV occurs simultaneously in the southern equatorial Indian Ocean between 70°-100°E, possibly associated with the thermohaline forcings. Spatial pattern at 100 m shows eastward propagation (arrows in Fig. 9b) and its amplitude become larger as it goes eastern boundary. Along the equatorial cross section the phase decreases with depth and increase with east indicating east-upward phase propagation (Fig. 9c), with the amplitude maxima along 100 m depth, consistent with STD of temperature ISV in Fig. 7c. This mode is consistent with equatorial Kelvin waves (Iskandar 2005; Schiller et al. 2010; Iskandar and McPhaden 2011). Figure 9d shows corresponding time series of phase and amplitude. The dominant period is about 54-day and the propagation speed decrease as depth; 2.16 m s^{-1} at the surface, 1.86 m s^{-1} at 100 m, and 1.00 m s^{-1} at 300 m. The propagation speed at 100 m depth, 1.86 m s^{-1}, is close to the 2nd baroclinic mode (1.67 m s^{-1}) (Moore and McCreary 1990). Large amplitude and long period events occur in boreal winter when MJO events tend to be stronger (Zhang 2005).

3.3. Regionally forced ISV

To quantify the relative importance of regional wind-stresses, we define Explained Variance Ratio (EVR) at each grid point as follows,

$$\mathrm{EVR}(x,y,z) = \left[\frac{1 - \frac{1}{t_2 - t_1}\int_{t_1}^{t_2} \left[u_{FF}(x,y,z,t) - u_{EXP}(x,y,z,t)\right]^2 dt}{\frac{1}{t_2 - t_1}\int_{t_1}^{t_2} u_{FF}(x,y,z,t)^2 dt} \right] \times 100\ (\%) \quad (2).$$

Here, again, x, y, and z are zonal, meridional and vertical coordinate, t is the time, u is band-pass filtered variable of interest, u_{FF} is the FF, u_{EXP} is the regional experiment. If the variance in FF is identical to that in the regional experiment, EVR is 100%.

Figure 10 shows EVRs of SST ISV. EVRs are quit large (>70%) around and south of equator over exactly the longitudinal range where wind-stress ISVs are retained in each experiments. This suggests that wind-stress affects ISV of SST locally. EVRs of 40-60% are found in regions where wind-tress ISV is eliminated, probably associated with thermohaline forcings. Note in regional forcing experiments only ISV wind-stress is suppressed, but heat and freshwater fluxes are not. These EVRs of 40-60% can be regarded as the contribution of other external forcings except wind-stress, then the contribution of wind-stress on ISV of SST is about 30%, smaller than that of other external forcings. Shortwave radiation and turbulent heat flux and vertical mixing by ISV of wind speed have been suggested as important factor of SST ISV in EEIO (Han et al. 2007; Duncan and Han 2009; Li et al. 2014; Chen et al. 2015; Horii et al. 2016). The EVRs are generally large to the south of the equator, probably because of the steep temperature gradient exist there (Figs. 3bd). Small EVRs in the off-equatorial regions in all experiments are consistent with the aforementioned dominance of the intrinsic variability to ISV in these regions (Fig. 5). In the equatorial Indian Ocean between 60° and 80°E, SST ISV is mostly explained by western wind-stress ISV (Fig. 10a). On the contrary, EVR of SST ISV for EF reaches 80% in the eastern equatorial band (80°-100°E) and narrow region along the Sumatra coast (Fig. 10b). Results of MidEF and FarEF indicate that ISV of SST in the eastern Equatorial band is well reproduced by wind forcing in MidEF (Figs. 10bcd). The narrow EVR maxima along the Sumatra southern coast in EF appear to be contributed from forcings in both MidEF and FarEF. This also indicates that local process is important in SST ISV along the Sumatra coast.

EVRs of temperature ISV at 100 m depth show distinct differences among experiments compared with EVRs of SST ISV (Fig. 11). Regions of 100 m temperature EVRs higher than 20% are much narrower than those for SST EVRs, and are generally limited along the equator and along the eastern boundary. Such differences are generally consistent with the difference of spatial structure of dominant forced response shown in Fig. 5. Very small EVR for FarEF west of 100°E (<10%), where wind-stress ISV is eliminate, indicates that the effect of external forcings except wind-stress on ISV of 100 m temperature is negligible (Fig. 11d). Western wind-stress dominantly explains 100 m temperature ISV (EVRs>50%) along the equatorial band between 65° and 95°E, whereas eastern wind-stress plays a dominant role along the equator east of 95°E and along the Sumatra and Java coast (Figs. 11ab). The most of features of EVR for EF are reproduced in MidEF (80°-100°E), while EVR for FarEF (east of 100°E) is generally small in the tropical Indian Ocean (Figs. 11cd). Only along the coast of Java wind-stress in FarEF contribute with similar magnitudes to those in MidEF to temperature ISV (Fig. 11bc).

To understand better how wind-forced ISV of temperature propagates to subsurface, EVRs are plotted along the equator-coast section (Fig. 12). Eastward and downward penetration of high EVRs are obvious in WF, EF and MidEF, consistent with energy propagation of equatorial and coastal Kelvin waves (Iskandar 2005; Schiller et al. 2010; Iskandar et al. 2014). Along the eastern equator between 80° and 100°E EVR of WF is larger than those of EF at 130 m or deeper depths (Figs. 12ab), thereby indicating the dominant role of remote wind-stress west of 80°E at those depths. This remote influence reaches to 500 m depth near the eastern boundary, and this localized deep penetration can be contribute not only Kelvin waves but reflected Rossby waves from the eastern boundary (Schiller et al. 2010; Nagura and McPhaden 2012). EVRs along the southern Sumatra coast in 0-200 m depth range are large in EF and MidEF, but small in FarEF (Figs. 12bcd).

This indicates that the remote forcings between 80° and 100°E substantially influence subsurface temperatures along the Sumatra coast. Along the southern Java coast, EVR is generally smaller than 10% in Fig. 12d, which is along the section of 500 m isobar, but higher EVR occurs nearer to the coast as seen in Fig. 11d. In the lower layer of western equator, EVRs are smaller than 10% in all panels, because temperature ISV in those regions is not caused by ISV of surface forcings (Fig. 5c). These results indicate that the how surface wind-stress causes remote ISV which depends the locations where equatorial Kelvin waves generated.

Wave propagation influences differently on different variables. Figure 13 shows EVRs of zonal velocity along the equator-coast cross section. Vertical penetration of large EVRs to the levels deeper than 100 m in zonal velocities is much weaker than that in temperatures. Eastward and downward penetration of large EVRs of zonal velocities occur in WF in the eastern equatorial Indian Ocean, somewhat similar to that seen for temperatures (Figs. 12a and 13a), but the former is located slightly to the west of the latter. This may be caused by the fact that the equatorial Kelvin waves and the reflected Rossby waves work destructively for zonal velocity but constructively for vertical displacements, which can contribute more effectively in temperatures. Also, high EVR in EF appear to penetrate downward and westward, consistent with energy propagation of long Rossby waves (Fig. 13b). The comparison of EVRs in MidEF and FarEF emphasizes the importance of wind-stress in MidEF (Figs. 13cd).

4. Summary and Discussion

In this study, the relative contribution of the intrinsic ISV and remote and local forcings on ISV in EEIO are investigated using 0.25° by 0.25° ROMS. We evaluate contributions of intrinsic and forced ISV, by conducting ensemble experiments, which have different initial perturbations for 10-year integrations with same atmospheric forcings and boundary conditions. Our model results reveal the dominance of intrinsic ISV in the western boundary region and the southern Indian Ocean especially in the subsurface (Fig. 5). In EEIO, intrinsic ISV is less than 30% of total ISV in whole 500 m depth, especially around the thermocline depth intrinsic ISV is one order of magnitude smaller than total ISV. In the region where the forced response is dominant, modeled SST and SSH ISVs are highly correlated with observed ones (Fig. 6), with the correlation coefficients larger than 0.5 in the central to eastern equatorial band, which is the pathway of equatorial and coastal Kelvin waves (Han 2005; Iskandar 2005; Iskandar et al. 2014). The spatial and temporal characteristics of temperature ISV in our model also suggest that Kelvin waves are highly related with forced ISV (Figs. 9). The amplitude (phase) of temperature ISV propagates east-downward (east-upward) along the equator. The propagation speed at 100 m depth is 1.86 m s^{-1} with 54-day period. These are close to the characteristics of 2nd baroclinic Kelvin wave (Moore and McCreary 1990).

The results in regional forcing experiments clearly indicate the role of wind-stress forcings in different regions in ISV in EEIO. At the surface, ISV of temperature mostly responds to local atmospheric forcings including heat and freshwater fluxes (Fig. 10). Most ISV of 100 m temperature can be explained by wind forcing; 50-60% by eastern wind, 30-40% by western wind, less than 10% by intrinsic ISV, and also less than 10% by other external forcing (Figs. 5c and 11). ISV of temperature by western forcing propagates eastward and downward, again consistent with energy propagation of Kelvin waves. The contribution of remote forcings (west of 80°E) becomes as large as local forcing about 130 m depth between 80°-100°E (Fig. 12). Western forcing propagating almost 500 m depth near the eastern boundary of equator causes almost half of temperature ISV. ISV of zonal velocity concentrates above the thermocline, hence vertical propagation of surface forcing is much weaker than that in temperature. Localized deep penetration of western forcings is found in the subsurface around 90°E, slightly west of that for temperature. Eastern forcing propagating west-downward and reaching almost 500 m depth around 85°E cannot be explained by only Kelvin waves; reflected Rossby waves from the eastern boundary also contribute ISV of subsurface zonal velocity (Han 2005; Nagura and McPhaden 2012).

Our model results further illustrate some interesting points of the forced and unforced response. First, the wind-stress forcings over different regions can act constructively or destructively or without specific relations. This can be examined by calculating correlation coefficients between temperature ISV in WF and that in EF. If forcings work constructively (destructively), correlations are positive (negative). If forcings work unrelated, correlations should be small. Second, more intense MJO and deeper thermocline in winter also may alter the relative role of forcings in different regions. The previous studies suggested that ISV itself has seasonality related with the seasonality of MJO and mean ocean state in EEIO (Chen et al. 2015; Horii et al. 2016). Thirdly, our approach to evaluate contribution of forced responses against those of the intrinsic ISV by calculating the ratio of inter-model difference to ISV of CNTL can be also used for interannual timescales. Finally, not only time variation but also mean state can be influenced by atmospheric ISV. Ogata et al. (2017) examined that ISV of wind stress contributes to increase mean vertical velocity along the equator of Indian Ocean. These four topics are discussed as follow.

Figure 14 shows the spatial patterns of correlation coefficient between temperature ISV in WF and that in EF. Although the correlation coefficients at 100 m depth is lower than 0.5 in whole Indian Ocean, relatively high values (>0.4) are found in EEIO and southwestern tropical Indian Ocean (Fig. 14a). There are no strongly negative (<-0.4) correlation coefficients in the whole domain. Correlation coefficients along the cross section (Fig. 14b) indicate that the relatively large correlations in EEIO centered at 130 m depth and 55 km from the western boundary or about 92°E, where the western forcing largely causes ISV of temperature with non-negligible contribution from the eastern forcing (Figs. 12ab). The high correlation coefficients found near the surface are possibly caused by the surface thermohaline forcings affecting ISV in broad area simultaneously (Fig 9).

Seasonal EVRs of temperatures ISV along the equator-coast cross section for WF and EF are shown in Fig. 15. Western forcing propagates east-downward in both boreal summer (June-September) and winter (December-February) but exhibit distinctive differences; in winter western forcing strongly influence 100-150 m depth range in EEIO, but penetrate deeper levels in summer with moderate EVRs (Figs. 15ac). Similarly, eastern forcings more strongly affect in the EEIO in winter than in summer (Figs. 15bd). Following the previous studies, we examine seasonality of wind stress and ocean mean state (Fig. 16). Along the equator, the zonal wind stress ISV increases in wintertime, intensifying the forced response at the surface. Near the southern coast of Sumatra and Java, both zonal and meridional wind-stress in winter distinctly has large values than that in summer. This can contribute the increase of temperature ISV in the subsurface along the Sumatra and Java. The seasonal pattern of STD of temperature ISV along the equator-coast cross section reveals the effect of seasonal upwelling. In summer, the wind forcing favors to upwell the subsurface water along the Sumatra and Java coast and in the southern tropical Indian Ocean. By contrast, upwelling occurs in western equatorial Indian Ocean in winter (Lévy et al. 2007). Correspondingly, 20°C isotherm depth and the depth range of the high STD of temperature fluctuate with season. The location of 20°C isotherm depth from 2000 km to 7000 km in winter matches up with the pathway of vertical propagation of temperature ISV (Figs. 15cd and 16d). The deep penetration of temperature ISV in summer cannot be explained directly from the patterns of wind-stress and temperature ISV.

Fig. 17 shows IVR of temperature and zonal velocity varying interannual timescale. Interannual variability is obtained as monthly anomalies from the monthly climatology. Overall, the portion of forced response becomes larger than that in intraseasonal timescale. For SST, IVR are smaller than 50% in most regions except the southeast region off the coast of Madagascar (Fig. 17a). The area of low IVR of interannual temperature (<30%) shrinks at 100 m depth than that at the surface, but still covering equatorial band, the center of the southern Indian Ocean, and the eastside of Bay of Bengal and Arabian Sea (Fig. 17c). Along the equator and the coast of Sumatra, the forced interannual variability of temperature overwhelms intrinsic variability in whole 500 m depth range. IVR smaller than 20% is found at 400-500 m depths not only east of 80°E but also 55°-60°E. This feature is much distinct in Fig. 17f, IVR of zonal velocity along the same section; IVR smaller than 20% propagates west-downward and reaches at 500 m depth in the western basin. This implies that in interannual timescale Rossby waves also play a major role in the variation of oceanic variable in the subsurface with Kelvin waves. IVR of interannual zonal velocity at the surface and 100 m depth is slightly wider than IVR of zonal velocity ISV, but the location of maxima is same (Figs. 5bd and 17bd). Relatively high IVR of interannual zonal velocity occupies the southeastern tropical Indian Ocean at both the surface and 100 m depth, consistent with the results of Ogata and Masumoto (2011), which reported that interannual variability in this region is caused by intrinsic variability by analyzing eddy-resolving model outputs.

Figure 18 shows the mean vertical velocity in FF and the difference of vertical velocity between FF and FarEF at 150 m. Mean upwelling appears along the equatorial band and western boundary region, consistent with Ogata et al. (2017), although the magnitude of mean vertical velocity in our model is significantly smaller. This can be induced by coarse horizontal resolution. Distinct differences in mean vertical velocity are found along 70°-90°E equatorial band and western boundary region, also consistent with Ogata et al. (2017). They suggested that increase of upwelling in EEIO by intraseasonal wind forcing from the results of vertical velocity forced by two different wind forcings; monthly climatological and daily wind stresses. Our model results reveal that removing only ISV of wind stress also can reduce upward vertical velocity.

Acknowledgements

I would like to record my gratitude to my supervisor, Professor Shoshiro Minobe. He has overseen the planning of this research and has given my work invaluable consideration for over three years. And a very special thanks to Lecturer Yoshinori Sasaki for detailed suggestions and technical assistance with numerical experiments. I wish to express my appreciation to my PhD committee, Professor Masaru Inatsu and Professor Youichi Tanimoto for useful comments and suggestions. Also many thanks go to Dr. Hiroyuki Tsujino, offering JRA55-DO data. It is a pleasure to acknowledge my debt to Dr. Hanna Na and Professor Humio Mitsudera discussing and encouraging my research. I thank all labmates, friendly, cheerful, and warm-hearted! Finally, I want to take this opportunity to thank my family, especially my parents, who have provided care, physical and emotional.

References

Balmaseda, M. A., K. Mogensen, and A. T. Weaver (2013) Evaluation of the ECMWF ocean reanalysis system ORAS4. Quarterly Journal of the Royal Meteorological Society 139(674):1132-1161. doi:10.1002/qj.2063

Banzon, V., T. M. Smith, T. M. Chin, C. Liu, and W. Hankins (2016) A long-term record of blended satellite and in situ sea-surface temperature for climate monitoring, modeling and environmental studies. Earth System Science Data 8(1):165-176. doi:10.5194/essd-8-165-2016

Brandt, P., M. Dengler, A. Rubino, D. Quadfasel, and F. Schott (2003) Intraseasonal variability in the southwestern Arabian Sea and its relation to the seasonal circulation. Deep Sea Research Part II: Topical Studies in Oceanography 50(12-13):2129-2141. doi:10.1016/s0967-0645(03)00049-3

Carton, J. A. (2005) Sea level rise and the warming of the oceans in the Simple Ocean Data Assimilation (SODA) ocean reanalysis. Journal of Geophysical Research 110(C9). doi:10.1029/2004jc002817

Carton, J. A., and B. S. Giese (2008) A Reanalysis of Ocean Climate Using Simple Ocean Data Assimilation (SODA). Monthly Weather Review 136(8):2999-3017. doi:10.1175/2007mwr1978.1

Chapman, D. C. (1985) Numerical treatment of cross-shelf open boundaries in a barotropic coastal ocean model. Journal of Physical oceanography 15(8):1060-1075

Chatterjee, A., D. Shankar, S. S. C. Shenoi, G. V. Reddy, G. S. Michael, M. Ravichandran, V. V. Gopalkrishna, E. P. R. Rao, T. V. S. U. Bhaskar, and V. N. Sanjeevan (2012) A new atlas of temperature and salinity for the North Indian Ocean. Journal of Earth System Science 121(3):559-593. doi:10.1007/s12040-012-0191-9

Chen, G., W. Han, Y. Li, D. Wang, and T. Shinoda (2015) Intraseasonal variability of upwelling in the equatorial Eastern Indian Ocean. Journal of Geophysical Research: Oceans 120(11):7598-7615. doi:10.1002/2015jc011223

Dai, A., and K. E. Trenberth (2002) Estimates of freshwater discharge from continents: Latitudinal and seasonal variations. Journal of hydrometeorology 3(6):660-687

Ducet, N., P. Y. Le Traon, and G. Reverdin (2000) Global high-resolution mapping of ocean circulation from TOPEX/Poseidon and ERS-1 and -2. Journal of Geophysical Research: Oceans 105(C8):19477-19498. doi:10.1029/2000jc900063

Duncan, B., and W. Han (2009) Indian Ocean intraseasonal sea surface temperature variability during boreal summer: Madden-Julian Oscillation versus submonthly forcing and processes. Journal of Geophysical Research 114(C5). doi:10.1029/2008jc004958

Duvel, J. P., R. Roca, and J. Vialard (2004) Ocean mixed layer temperature variations induced by intraseasonal convective perturbations over the Indian Ocean. Journal of the atmospheric sciences 61(9):1004-1023

Egbert, G. D., and S. Y. Erofeeva (2002) Efficient inverse Modeling of barotropic ocean tides. Journal of Atmospheric and Oceanic Technology 19(2):183-204. doi:10.1175/1520-0426(2002)019<0183:eimobo>2.0.co;2

Fairall, C., E. F. Bradley, J. Hare, A. Grachev, and J. Edson (2003) Bulk parameterization of air–sea fluxes: Updates and verification for the COARE algorithm. Journal of climate 16(4):571-591

Feng, M., and S. Wijffels (2002) Intraseasonal variability in the South Equatorial Current of the east Indian Ocean. Journal of physical oceanography 32(1):265-277

Flather, R. (1976) A tidal model of the northwest European continental shelf. Mem. Soc. R. Sci. Liege 10(6):141-164

Garcia, H., R. Locarnini, T. Boyer, and J. Antonov (2010) World Ocean Atlas 2009, vol. 4, Nutrients (Phosphate, Nitrate, Silicate), NOAA Atlas NESDIS, vol. 71. US Gov. Print. Off., Washington, DC

Guan, B., T. Lee, D. J. Halkides, and D. E. Waliser (2014) Aquarius surface salinity and the Madden-Julian Oscillation: The role of salinity in surface layer density and potential energy. Geophysical Research Letters 41(8):2858-2869. doi:10.1002/2014gl059704

Haidvogel, D. B., H. G. Arango, K. Hedstrom, A. Beckmann, P. Malanotte-Rizzoli, and A. F. Shchepetkin (2000) Model evaluation experiments in the North Atlantic Basin: simulations in nonlinear terrain-following coordinates. Dynamics of Atmospheres and Oceans 32(3):239-281

Han, W. (2005) Origins and dynamics of the 90-day and 30–60-day variations in the equatorial Indian Ocean. Journal of physical oceanography 35(5):708-728

Han, W., D. Yuan, W. T. Liu, and D. J. Halkides (2007) Intraseasonal variability of Indian Ocean sea surface temperature during boreal winter: Madden-Julian Oscillation versus submonthly forcing and processes. Journal of Geophysical Research 112(C4). doi:10.1029/2006jc003791

Harada, Y., H. Kamahori, C. Kobayashi, H. Endo, S. Kobayashi, Y. Ota, H. Onoda, K. Onogi, K. Miyaoka, and K. Takahashi (2016) The JRA-55 Reanalysis: Representation of

Atmospheric Circulation and Climate Variability. Journal of the Meteorological Society of Japan. Ser. II 94(3):269-302. doi:10.2151/jmsj.2016-015

Harrison, D. E., and G. A. Vecchi (2001) January 1999 Indian Ocean Cooling Event. Geophysical Research Letters 28(19):3717-3720. doi:10.1029/2001gl013506

Horii, T., I. Ueki, F. Syamsudin, I. Sofian, and K. Ando (2016) Intraseasonal coastal upwelling signal along the southern coast of Java observed using Indonesian tidal station data. Journal of Geophysical Research: Oceans 121(4):2690-2708. doi:10.1002/2015jc010886

Horii, T., I. Ueki, K. Ando, T. Hasegawa, K. Mizuno, and A. Seiki (2015) Impact of intraseasonal salinity variations on sea surface temperature in the eastern equatorial Indian Ocean. Journal of Oceanography 72(2):313-326. doi:10.1007/s10872-015-0337-x

Iskandar, I. (2005) Intraseasonal Kelvin waves along the southern coast of Sumatra and Java. Journal of Geophysical Research 110(C4). doi:10.1029/2004jc002508

Iskandar, I., and M. J. McPhaden (2011) Dynamics of wind-forced intraseasonal zonal current variations in the equatorial Indian Ocean. Journal of Geophysical Research 116(C6). doi:10.1029/2010jc006864

Iskandar, I., Y. Masumoto, K. Mizuno, H. Sasaki, A. K. Affandi, D. Setiabudidaya, and F. Syamsuddin (2014) Coherent intraseasonal oceanic variations in the eastern equatorial Indian Ocean and in the Lombok and Ombai Straits from observations and a high-resolution OGCM. Journal of Geophysical Research: Oceans 119(2):615-630

Jin, D., R. Murtugudde, and D. E. Waliser (2012a) Tropical Indo-Pacific Ocean chlorophyll response to MJO forcing. Journal of Geophysical Research: Oceans 117(C11):n/a-n/a. doi:10.1029/2012jc008015

Jin, D., D. E. Waliser, C. Jones, and R. Murtugudde (2012b) Modulation of tropical ocean surface chlorophyll by the Madden–Julian Oscillation. Climate Dynamics 40(1-2):39-58. doi:10.1007/s00382-012-1321-4

Keerthi, M. G., M. Lengaigne, J. Vialard, C. de Boyer Montégut, and P. M. Muraleedharan (2012) Interannual variability of the Tropical Indian Ocean mixed layer depth. Climate Dynamics 40(3-4):743-759. doi:10.1007/s00382-012-1295-2

Keerthi, M. G., M. Lengaigne, K. Drushka, J. Vialard, C. de Boyer Montegut, S. Pous, M. Levy, and P. M. Muraleedharan (2015) Intraseasonal variability of mixed layer depth in the tropical Indian Ocean. Climate Dynamics 46(7-8):2633-2655. doi:10.1007/s00382-015-2721-z

Kobayashi, C., and T. Iwasaki (2016) Brewer-Dobson circulation diagnosed from JRA-55. Journal of Geophysical Research: Atmospheres 121(4):1493-1510. doi:10.1002/2015jd023476

Le Traon, P. Y., F. Nadal, and N. Ducet (1998) An improved mapping method of multisatellite altimeter data. Journal of Atmospheric and Oceanic Technology 15(2):522-534. doi:10.1175/1520-0426(1998)015<0522:aimmom>2.0.co;2

Lévy, M., D. Shankar, J. M. André, S. S. C. Shenoi, F. Durand, and C. de Boyer Montégut (2007) Basin-wide seasonal evolution of the Indian Ocean's phytoplankton blooms. Journal of Geophysical Research 112(C12). doi:10.1029/2007jc004090

Li, Y., W. Han, and T. Lee (2015) Intraseasonal sea surface salinity variability in the equatorial Indo-Pacific Ocean induced by Madden-Julian oscillations. Journal of Geophysical Research: Oceans 120(3):2233-2258

Li, Y., W. Han, T. Shinoda, C. Wang, M. Ravichandran, and J.-W. Wang (2014) Revisiting the Wintertime Intraseasonal SST Variability in the Tropical South Indian Ocean: Impact of the Ocean Interannual Variation*. Journal of Physical Oceanography 44(7):1886-1907. doi:10.1175/jpo-d-13-0238.1

Mellor, G. L., and T. Yamada (1982) Development of a turbulence closure model for geophysical fluid problems. Reviews of Geophysics 20(4):851-875

Mogensen, K., M. A. Balmaseda, and A. Weaver (2012) The NEMOVAR ocean data assimilation system as implemented in the ECMWF ocean analysis for System 4. European Centre for Medium-Range Weather Forecasts

Moore, D. W., and J. P. McCreary (1990) Excitation of intermediate-frequency equatorial waves at a western ocean boundary: With application to observations from the Indian Ocean. Journal of Geophysical Research 95(C4):5219. doi:10.1029/JC095iC04p05219

Nagura, M., and M. J. McPhaden (2012) The dynamics of wind-driven intraseasonal variability in the equatorial Indian Ocean. Journal of Geophysical Research: Oceans 117(C2):n/a-n/a. doi:10.1029/2011jc007405

Ogata, T., and Y. Masumoto (2011) Interannual modulation and its dynamics of the mesoscale eddy variability in the southeastern tropical Indian Ocean. Journal of Geophysical Research 116(C5). doi:10.1029/2010jc006490

Ogata, T., M. Nagura, and Y. Masumoto (2017) Mean Subsurface Upwelling Induced by Intraseasonal Variability over the Equatorial Indian Ocean. Journal of Physical Oceanography 47(6):1347-1365. doi:10.1175/jpo-d-16-0257.1

Ogata, T., H. Sasaki, V. S. N. Murty, M. S. S. Sarma, and Y. Masumoto (2008) Intraseasonal meridional current variability in the eastern equatorial Indian Ocean. Journal of Geophysical Research 113(C7). doi:10.1029/2007jc004331

Oliver, E. C. J., and K. R. Thompson (2010) Madden-Julian Oscillation and sea level: Local and remote forcing. Journal of Geophysical Research 115(C1). doi:10.1029/2009jc005337

Palastanga, V., P. J. van Leeuwen, M. W. Schouten, and W. P. M. de Ruijter (2007) Flow structure and variability in the subtropical Indian Ocean: Instability of the South Indian Ocean Countercurrent. Journal of Geophysical Research 112(C1). doi:10.1029/2005jc003395

Paulson, C. A., and J. J. Simpson (1977) Irradiance measurements in the upper ocean. Journal of Physical Oceanography 7(6):952-956

Raj Parampil, S., G. Bharathraj, M. Harrison, and D. Sengupta (2016) Observed subseasonal variability of heat flux and the SST response of the tropical Indian Ocean. Journal of Geophysical Research: Oceans 121(10):7290-7307

Resplandy, L., J. Vialard, M. Lévy, O. Aumont, and Y. Dandonneau (2009) Seasonal and intraseasonal biogeochemical variability in the thermocline ridge of the southern tropical Indian Ocean. Journal of Geophysical Research 114(C7). doi:10.1029/2008jc005246

Reynolds, R. W., T. M. Smith, C. Liu, D. B. Chelton, K. S. Casey, and M. G. Schlax (2007) Daily high-resolution-blended analyses for sea surface temperature. Journal of Climate 20(22):5473-5496

Saji, N. H., S. P. Xie, and C. Y. Tam (2006) Satellite observations of intense intraseasonal cooling events in the tropical south Indian Ocean. Geophysical Research Letters 33(14). doi:10.1029/2006gl026525

Schiller, A., and P. R. Oke (2015) Dynamics of ocean surface mixed layer variability in the Indian Ocean. Journal of Geophysical Research: Oceans 120(6):4162-4186. doi:10.1002/2014jc010538

Schiller, A., S. E. Wijffels, J. Sprintall, R. Molcard, and P. R. Oke (2010) Pathways of intraseasonal variability in the Indonesian Throughflow region. Dynamics of Atmospheres and Oceans 50(2):174-200. doi:10.1016/j.dynatmoce.2010.02.003

Schott, F. A., and J. P. McCreary (2001) The monsoon circulation of the Indian Ocean. Prog Oceanogr 51(1):1-123

Sengupta, D., R. Senan, and B. N. Goswami (2001) Origin of intraseasonal variability of circulation in the tropical central Indian Ocean. Geophysical Research Letters 28(7):1267-1270. doi:10.1029/2000gl012251

Shchepetkin, A. F., and J. C. McWilliams (2005) The regional oceanic modeling system (ROMS): a split-explicit, free-surface, topography-following-coordinate oceanic model. Ocean Modelling 9(4):347-404. doi:10.1016/j.ocemod.2004.08.002

Song, Y., and D. Haidvogel (1994) A semi-implicit ocean circulation model using a generalized topography-following coordinate system. Journal of Computational Physics 115(1):228-244

Umlauf, L., and H. Burchard (2003) A generic length-scale equation for geophysical turbulence models. Journal of Marine Research 61(2):235-265

Waliser, D. E., R. Murtugudde, P. Strutton, and J.-L. Li (2005) Subseasonal organization of ocean chlorophyll: Prospects for prediction based on the Madden-Julian Oscillation. Geophysical Research Letters 32(23). doi:10.1029/2005gl024300

Webber, B. G., A. J. Matthews, K. J. Heywood, J. Kaiser, and S. Schmidtko (2014) Seaglider observations of equatorial Indian Ocean Rossby waves associated with the Madden-Julian Oscillation. Journal of Geophysical Research: Oceans 119(6):3714-3731

Webster, P. J., and R. Lukas (1992) TOGA COARE: The coupled ocean—atmosphere response experiment. Bulletin of the American Meteorological Society 73(9):1377-1416

Yu, Z., and J. Potemra (2006) Generation mechanism for the intraseasonal variability in the Indo-Australian basin. Journal of Geophysical Research 111(C1). doi:10.1029/2005jc003023

Zhang, C. (2005) Madden-Julian Oscillation. Reviews of Geophysics 43(2). doi:10.1029/2004rg000158

Zhou, L., R. Murtugudde, and M. Jochum (2008) Dynamics of the Intraseasonal Oscillations in the Indian Ocean South Equatorial Current. Journal of Physical Oceanography 38(1):121-132. doi:10.1175/2007jpo3730.1

Table

Table 1. The list of experiments.

Experiments	Long Name	Spin-up time
CNTL	Control run	1996.01.01-2005.12.31 (10 years)
E2	2nd ensemble	1996.01.01-2004.12.31 (9 years)
E3	3rd ensemble	1996.01.01-2003.12.31 (8 years)
Experiments	**Long Name**	**Longitude range where wind-stress has intraseasonal variability**
FF (=CNTL)	Full Forcing run	30°-120°E (whole domain)
WF	Western Forcing run	30°-80°E
EF	Eastern Forcing run	80°-120°E
MidEF	Middle Eastern Forcing run	80°-100°E
FarEF	Far Eastern Forcing run	100°-120°E

Figures

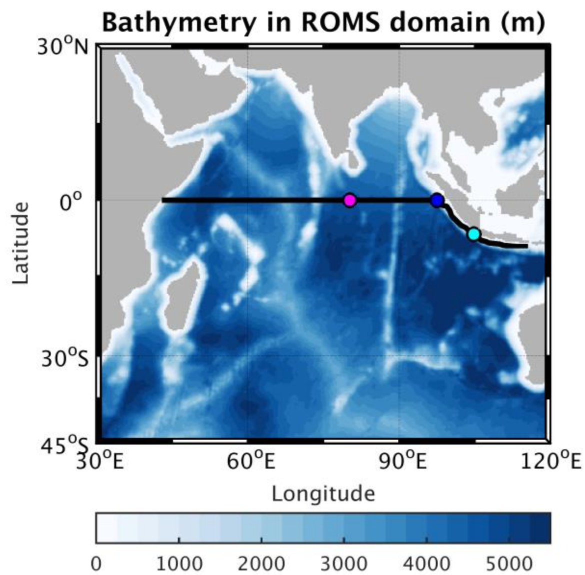

Figure 1. Bathymetry in ROMS domain. Black line shows the section along the equator and 500 m isobar to the south of islands (equator-coast cross section). Pink, blue, and cyan dots indicate (0°, 80°E), (0°, 98.75°E), and (6.03°S, 105.25°E), respectively.

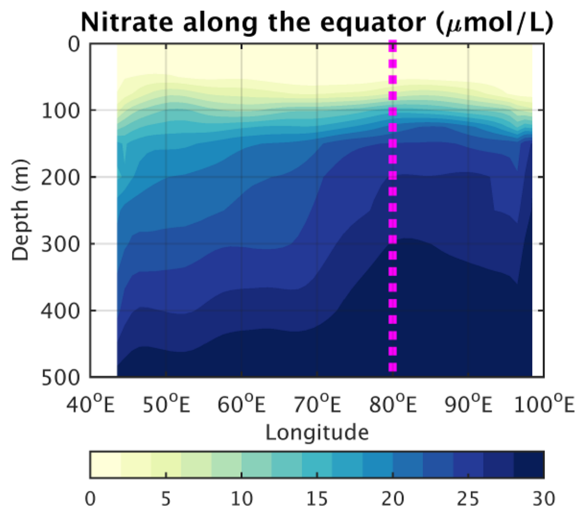

Figure 2. Climatological nitrate concentration along the equator. Pink line indicates the location of pink dot in Fig. 1.

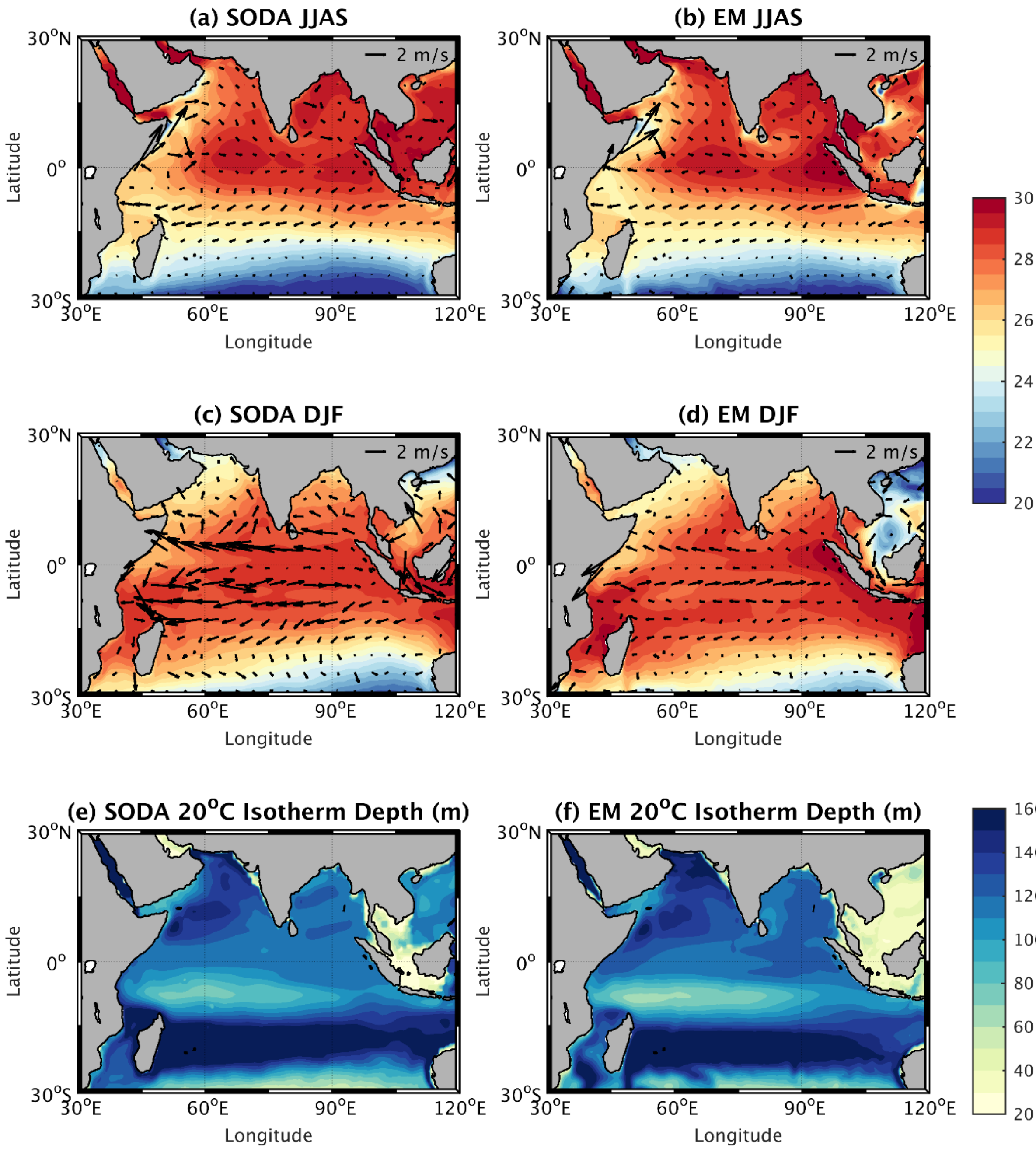

Figure 3. Summer (JJAS) and winter (DJF) mean temperature (color, °C) and current at 10 m depth (vector) from (a and c) SODA and (b and d) EM. Annual mean 20°C isotherm depth from (e) SODA and (f) EM.

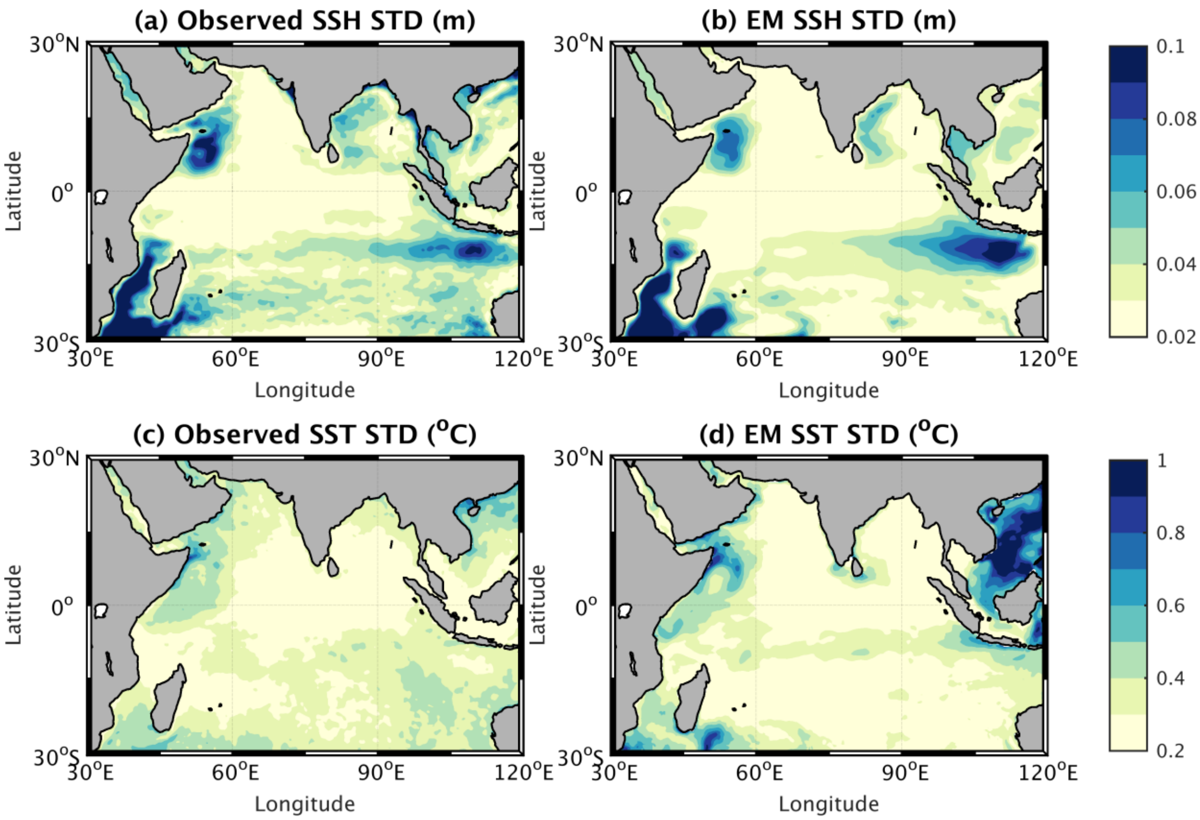

Figure 4. Comparison of observed and modeled ISV. STD of SSH is given from (a) AVISO and (b) EM. STD of SST is given from (c) OISST and (d) EM.

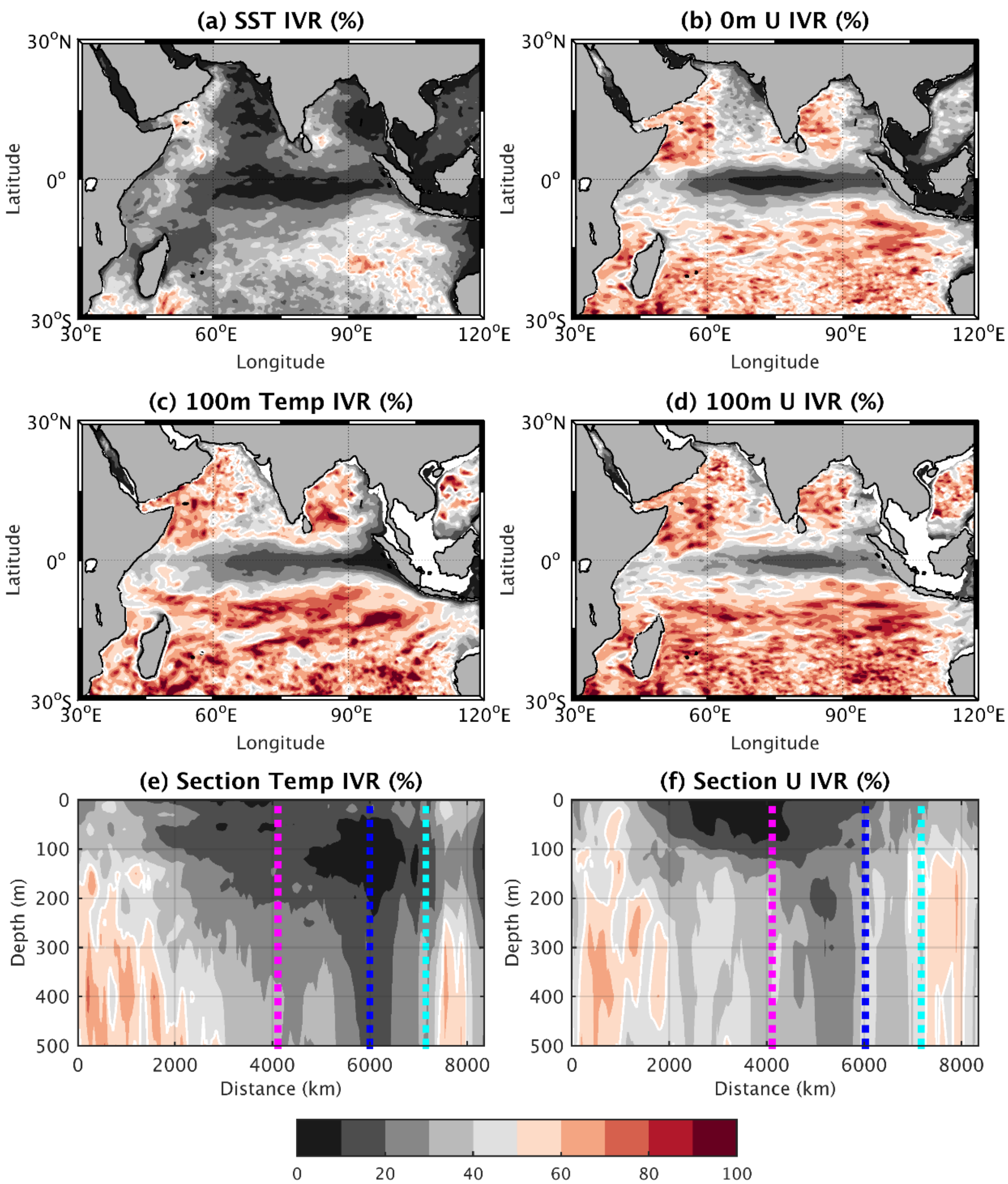

Figure 5. IVRs of temperature and zonal velocity. Panel (a), (c), and (e) shows IVRs of temperature at 0 m, 100 m, and along the equator-coast cross section in Fig. 1. Panel (b), (d), and (f) are same as panel (a), (c), and (e) but zonal velocity. White contour indicates the region where IVRs are 50%. X axis of panel (e) and (f) is the distance from western boundary of equatorial Indian Ocean (43.5°E). Pink, blue, and cyan lines indicate the locations of same color dots in Fig. 1.

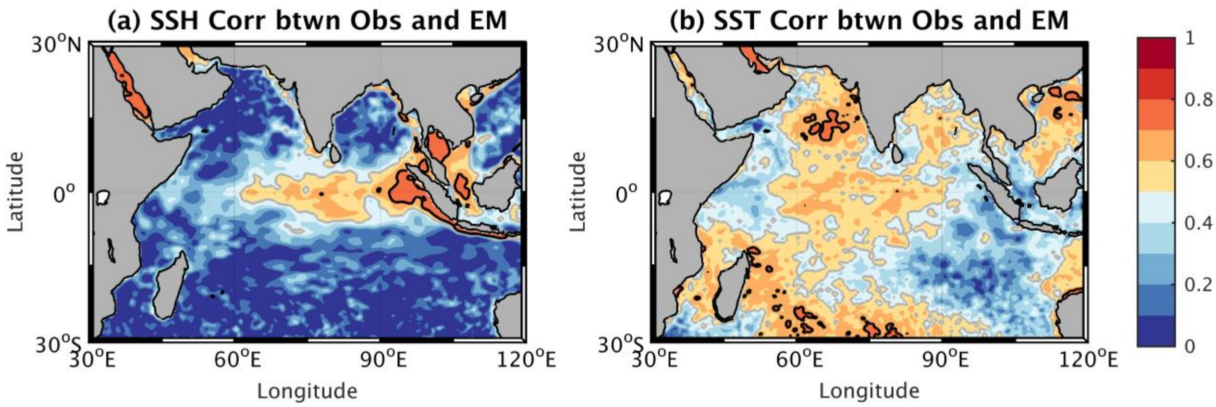

Figure 6. Correlation map between observed and modeled ISV. Panel (a) shows correlation coefficients between SSH in AVISO and that in EM. Panel (b) shows correlation coefficients between SST in OISST and that in ensemble mean. Gray (black) contour indicates the region where correlation coefficients are 0.5 (0.7).

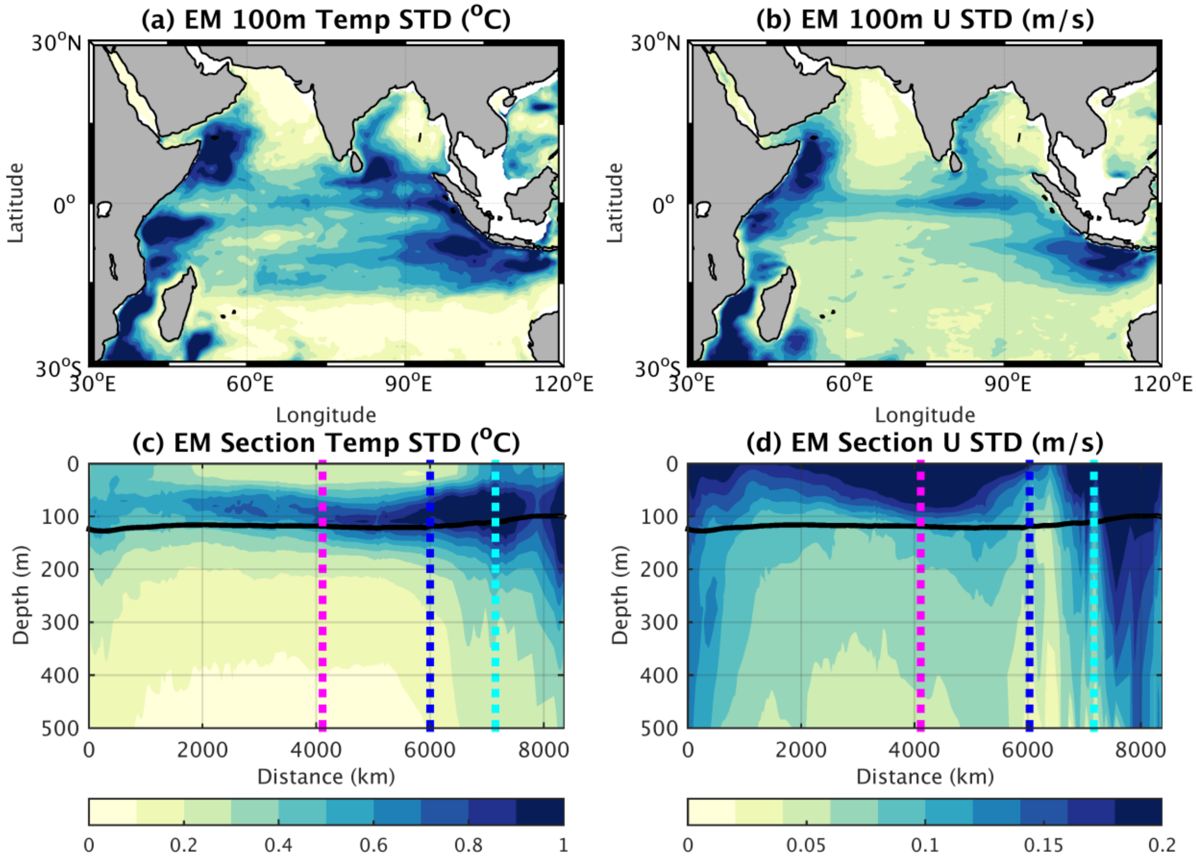

Figure 7. STD of temperature and zonal velocity ISV in EM. Panel (a) and (c) show ISV of temperature at 100 m depth and along the equator-coast cross section in Fig. 1. Panel (b) and (d) are same as panel (a) and (c) but ISV of zonal velocity. X axis of panel (c) and (d) is the distance from western boundary of equatorial Indian Ocean (43.5°E). Black line shows annual mean 20°C isotherm depth. Pink, blue, and cyan lines indicate the locations of same color dots in Fig. 1.

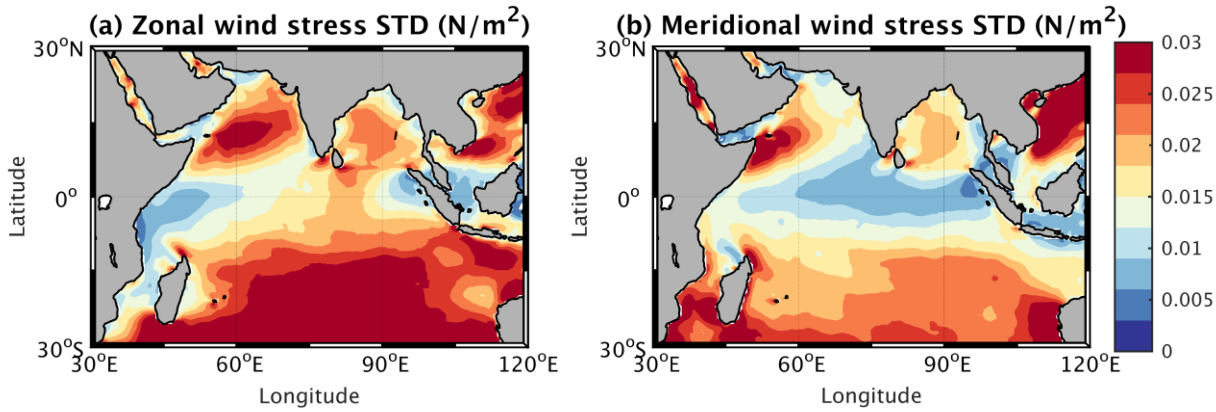

Figure 8. STD of ISV of (a) zonal and (b) meridional wind-stress in JRA55-DO.

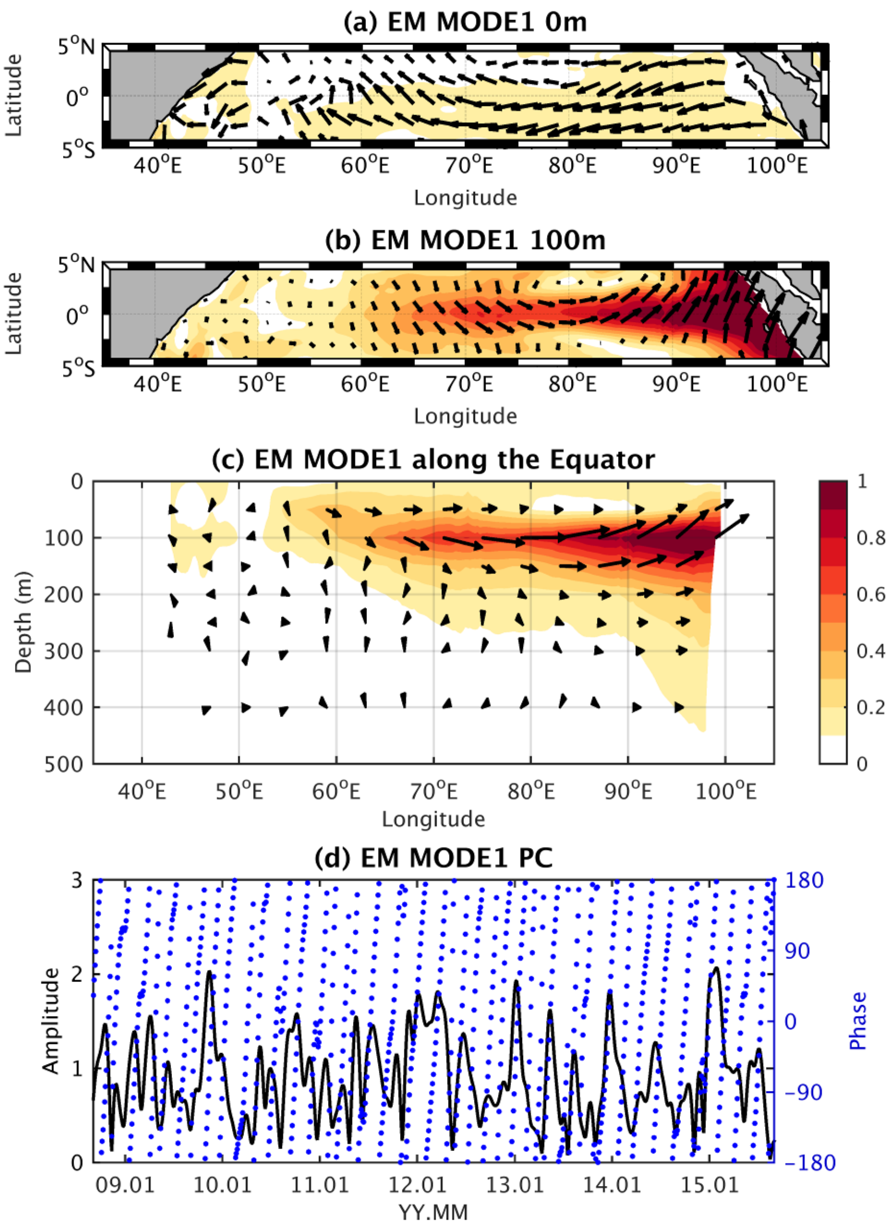

Figure 9. CEOF first mode spatial patterns of the amplitude (color) and the phase (vector) using ISV of temperature in EM at (a) 0 m, (d) 100 m, and (c) along the equator. Panel (d) shows the amplitude (black solid line) and the phase (blue dotted line) of the first principal component. The arrow pointing to the right indicates 0° phase, and the phase increases in the direction of arrow rotating counterclockwise. The arrow length is proportional to the amplitude.

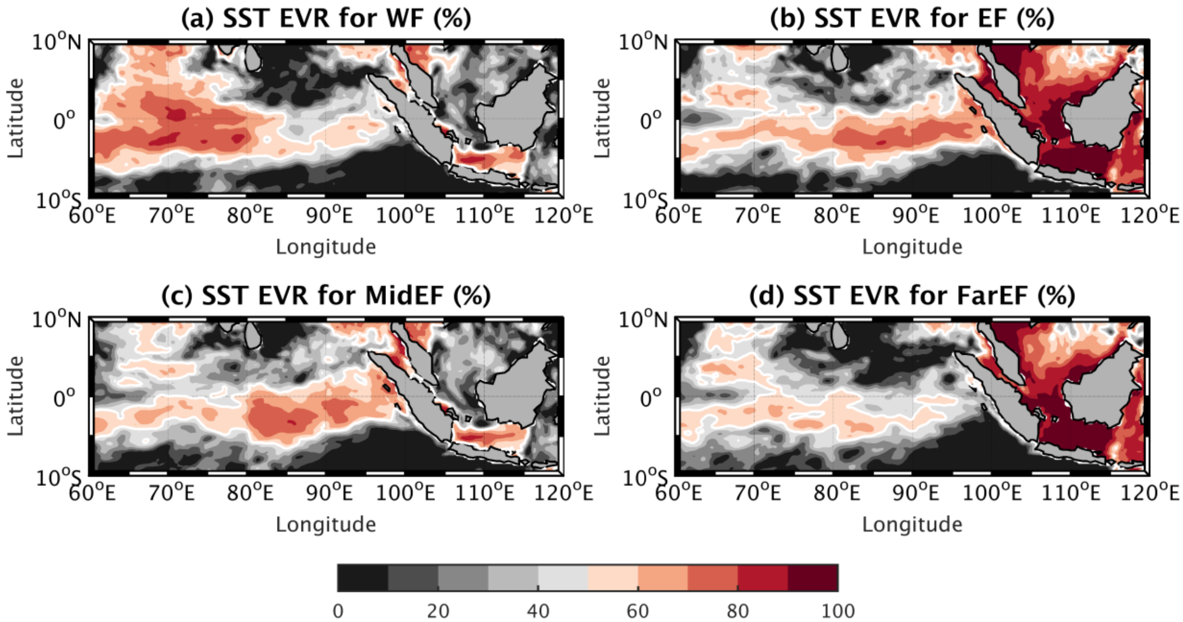

Figure 10. EVRs of SST ISV for (a) WF, (b) EF, (c) MidEF, and (d) FarEF. White contour denotes 50%.

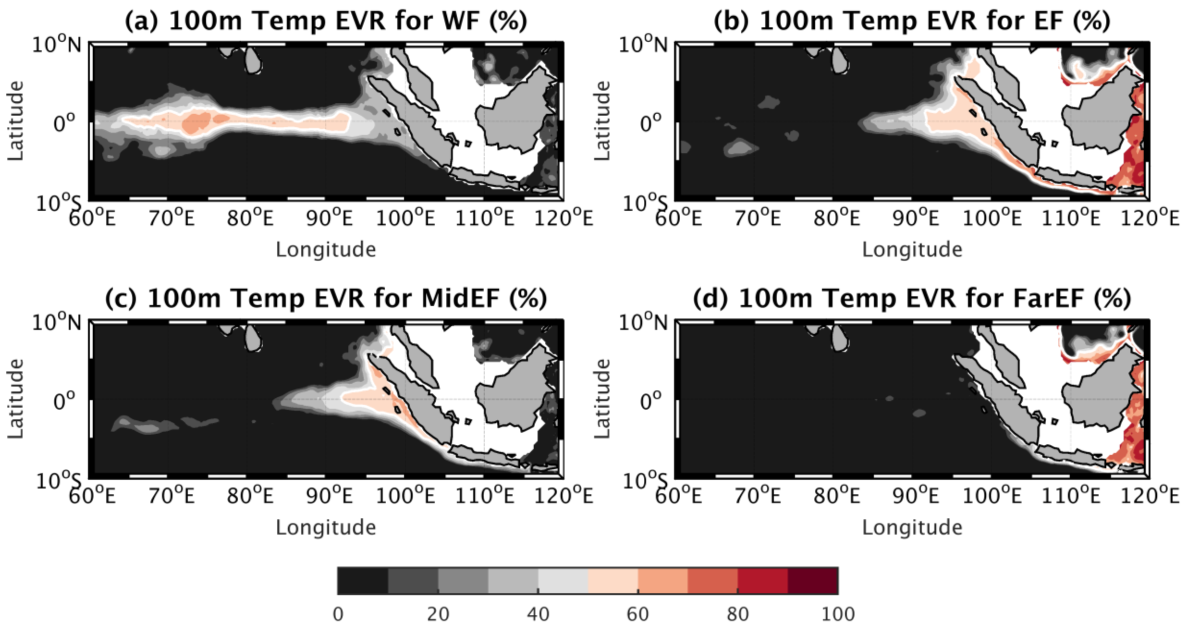

Figure 11. As in Fig. 10, but EVRs of temperature ISV at 100 m.

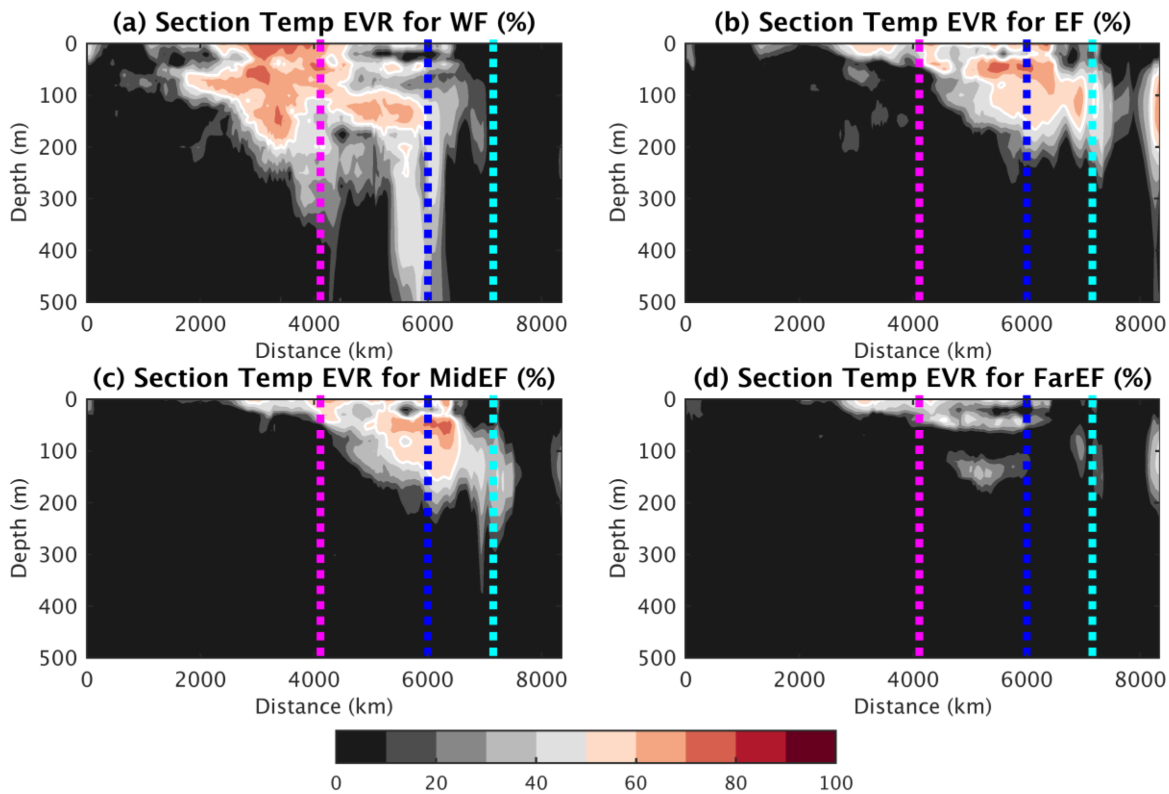

Figure 12. As in Fig. 10, but EVRs of temperature ISV along the equator-coast cross section in Fig. 1. X axis is the distance from western boundary of equatorial Indian Ocean (43.5°E). Pink, blue, and cyan lines indicate the locations of same color dots in Fig. 1.

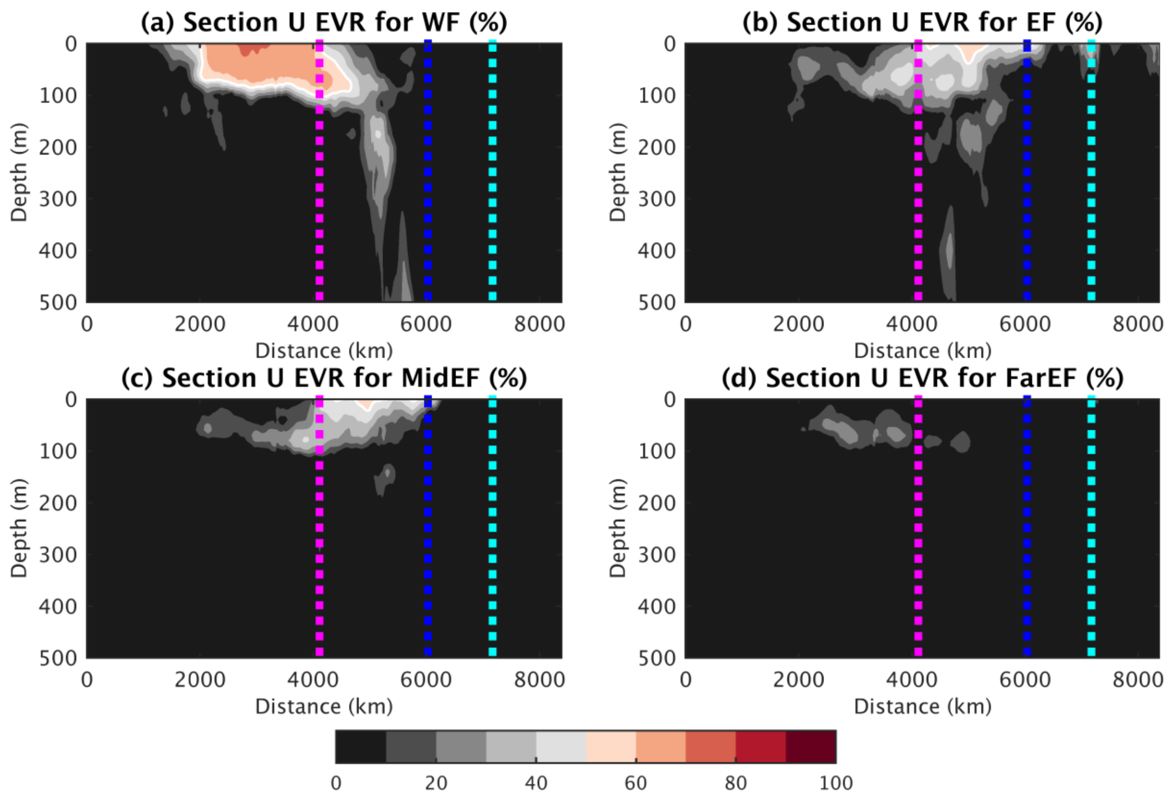

Figure 13. As in Fig. 12, but EVRs of zonal velocity ISV.

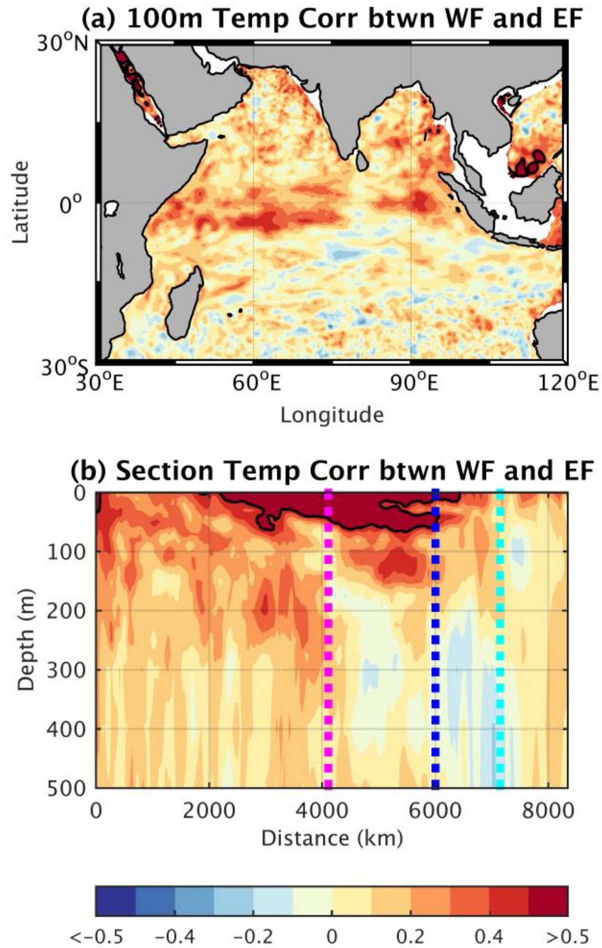

Figure 14. Correlation coefficients of temperature ISV (a) at 100 m depth and (b) along the equator-coast cross section in Fig. 1 between WF and EF. Black contour indicates the region where correlation coefficients are 0.5. X axis in panel (b) is the distance from western boundary of equatorial Indian Ocean (43.5°E). Pink, blue, and cyan lines indicate the locations of same color dots in Fig. 1.

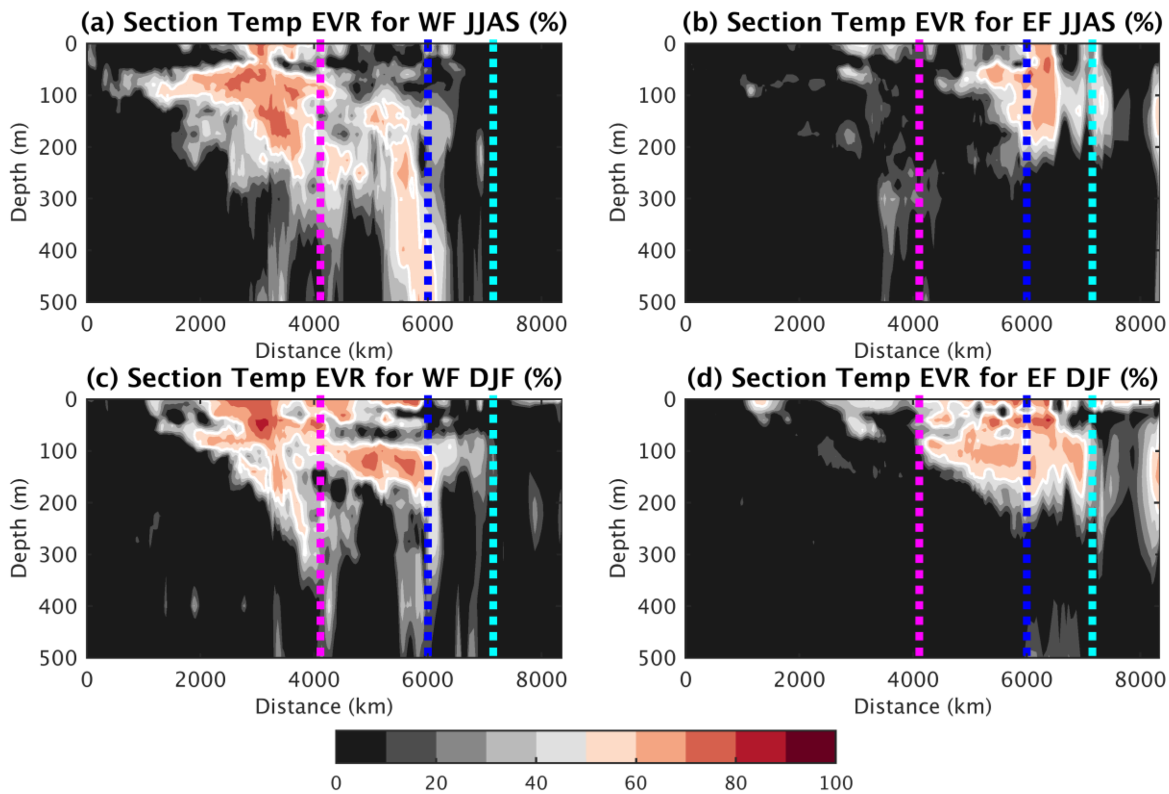

Figure 15. EVRs of temperature ISV along the equator-coast cross section in Fig. 1 for WF (a) in summer (JJAS) and (c) in winter (DJF) and for EF (b) in summer and (d) in winter (DJF). X axis is the distance from western boundary of equatorial Indian Ocean (43.5°E). Pink, blue, and cyan lines indicate the locations of same color dots in Fig. 1.

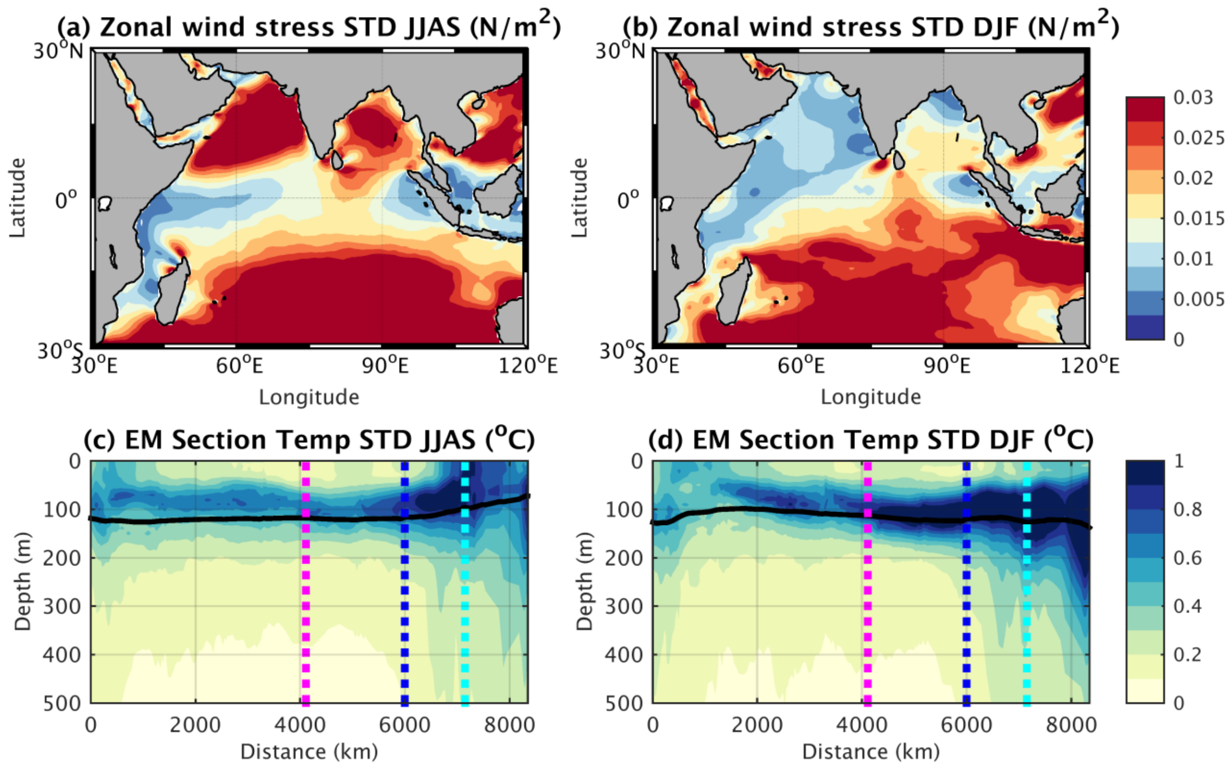

Figure 16. STD of zonal wind-stress ISV in (a) summer (JJAS) and (b) winter (DJF) and temperature ISV in (c) summer and (d) winter. X axis in panel (c) and (d) is the distance from western boundary of equatorial Indian Ocean (43.5°E). Pink, blue, and cyan lines indicate the locations of same color dots in Fig. 1.

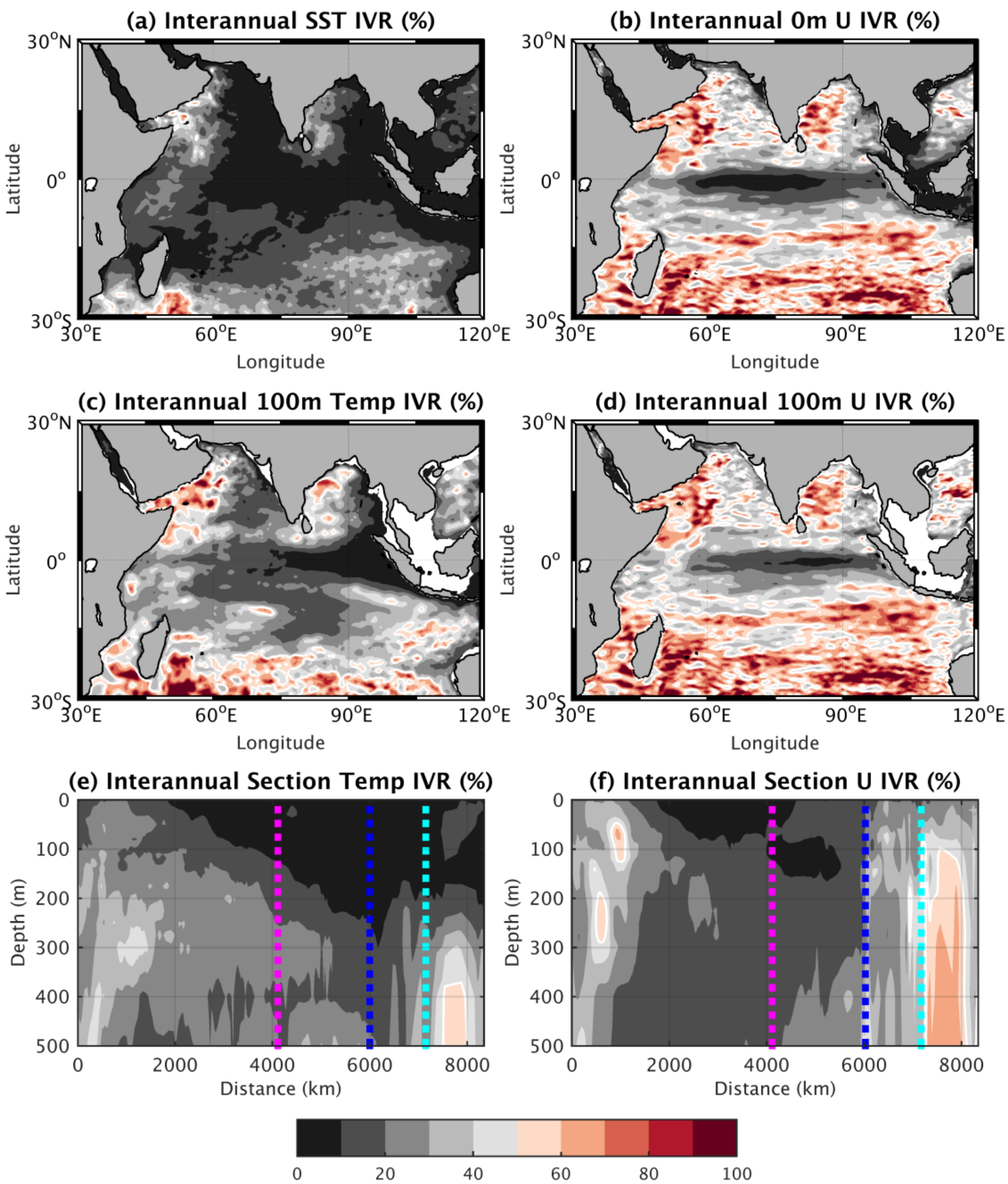

Figure 17. As in Fig. 5, but IVRs of interannual variability of temperature and zonal velocity.

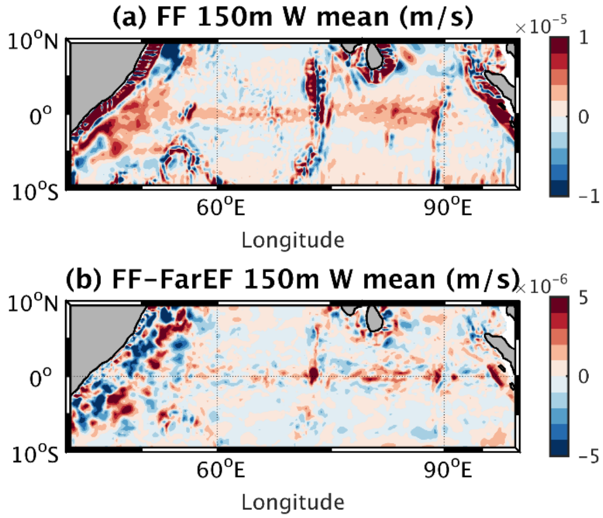

Figure 18. Mean vertical velocity comparison at 150 m. Panel (a) shows mean vertical velocity in FF. Panel (b) shows the difference of mean vertical velocity between FF and FarEF.